Conduction Modelling Using Smoothed Particle Hydrodynamics

Paul W. Cleary* and Joseph J. Monaghan†

Division of Mathematical and Information Sciences, CSIRO, Private Bag 10, South Clayton MDC, Victoria, 3169, Australia; and †Department of Mathematics and Statistics, Monash University, Clayton, Victoria, 3168, Australia
E-mail: *Paul.Cleary@cmis.csiro.au and †Joe.Monaghan@sci.monash.edu.au

Heat transfer is very important in many industrial and geophysical problems. Because these problems often have complicated fluid dynamics, there are advantages in solving them using Lagrangian methods like smoothed particle hydrodynamics (SPH). Since SPH particles become disordered, the second derivative terms may be estimated poorly, especially when materials with different properties are adjacent. In this paper we show how a simple alteration to the standard SPH formulation ensures continuity of heat flux across discontinuities in material properties. A set of rules is formulated for the construction of isothermal boundaries leading to accurate conduction solutions. A method for accurate prediction of heat fluxes through isothermal boundaries is also given. The accuracy of the SPH conduction solutions is demonstrated through a sequence of test problems of increasing complexity.   © 1999 Academic Press

1. INTRODUCTION

Many of the problems of geophysical and industrial fluid dynamics involve complex flows. A typical example is a process involving more than one material and more than one phase with interfaces which may lead to wave breaking and splash. Thermal and chemical processes present further complications.

The simulation of such systems can sometimes present difficulties for finite difference and finite element methods, particularly when coupled with complex free surface motion. For example, the relatively simple problem of a wave overturning and breaking on a free surface can only be followed with these methods until the overturning wave touches the fluid [10]. By comparison, smoothed particle hydrodynamics (SPH) (for a review see [11]) can easily follow wave breaking. Furthermore it provides a reasonable simulation of splash on a length scale exceeding that where surface tension must be included [13].

227

The flexibility of SPH arises because a grid is not needed except as a bookkeeping device. Derivatives are calculated by exactly differentiating an interpolation formula. However, the greater the disorder of the particles, the less accurate the derivatives, and second and higher derivatives must be treated with particular care. For example, a successful SPH algorithm for simulating the dynamics of fluids, including liquid metals, in which thermal conduction is important, requires a robust method of calculating second derivatives. Brookshaw [2] proposed one such method and his numerical experiments confirmed that it worked well for problems with constant or slowly varying thermal conductivity. However, in many industrial problems the thermal conductivity can change rapidly, or even discontinuously, because different materials (for example, air and metal) are in contact. The form of the heat conduction equation given by Brookshaw does not work well in these cases because it does not ensure continuity of the heat flux.

In this paper we describe an SPH algorithm for heat conduction which works well even when the thermal conductivity changes discontinuously or is a sensitive function of the temperature. Conductivity ratios of up to 1000:1 between adjacent materials were tested successfully. We also show how to construct boundary conditions so that the flux of heat across the boundary is accurate. To confirm that our method is not sensitive to the particle configuration we also apply the algorithm to configurations where the boundaries are straight but not aligned with the particles, where the boundaries are curved and where the particle positions are those that occur in a dynamical simulation. In all cases the algorithm produces very accurate results.

This SPH algorithm for accurately treating heat conduction was developed so that the method could be applied to complex industrial free surface flow problems involving heat transfer, such as multi-material flows in electric arc furnaces and high-pressure die casting of metal automotive components. Even though the ultimate aim of this work is to apply the heat transfer method to nonisothermal free surface flows, it is necessary that it be able to accurately predict conduction in solids with strongly varying and discontinuous material properties in configurations of geometric complexity. If one were principally interested in solving heat conduction in solids then more conventional fixed grid or mesh methods would be more suitable.

For coupled heat and fluid flows where there are large deformations in the material boundaries, the SPH method offers significant advantages over conventional methods. Demonstrating the accuracy of these solutions is well beyond the scope of the present paper (partly because of the difficulty in obtaining either numerical or experimental results with which to compare them and partly because simulation of pure conduction is already a significant advance). SPH has been shown to also give results which agree well with high-accuracy finite element solutions for natural convection in a cavity at low and medium Rayleigh numbers [5], suggesting that the jump to the more complex flows is unlikely to be difficult for this method.

2. THE SPH METHOD

A review of SPH is given in [11]. This describes briefly the connection to earlier particle methods and the overall methodology. Here we are interested in the construction of SPH equations that correspond to the thermal energy equation. For SPH calculations we assume the medium and the boundary are represented by a set of particles. Particle a has mass m_a, density ρ_a, thermal conductivity k_a, temperature T_a, energy per unit mass u_a, and position $\mathbf{r_a}$.

The interpolated value of a function A at position $\mathbf{r}$ is given by

$$A(\mathbf{r}) = \sum_b m_b \frac{A_b}{\rho_b} W(\mathbf{r} - \mathbf{r}_b, h), \tag{1}$$

where W is a spline based interpolation kernel of radius $2h$ and the summation occurs over all particles b within the radius of the kernel centered on position $\mathbf{r}$ (see [11] for details).

The gradient of the function A can be obtained by analytically differentiating the interpolation formula (1). Thus,

$$\nabla A(\mathbf{r}) = \sum_b m_b \frac{A_b}{\rho_b} \nabla W(\mathbf{r} - \mathbf{r}_b, h). \tag{2}$$

Since the kernels are similar in form and symmetry to a Gaussian we can always write

$$\nabla W_{ab} = \mathbf{r}_{ab} F_{ab}, \tag{3}$$

where $\mathbf{r}_{ab} = \mathbf{r}_a - \mathbf{r}_b$ and F_{ab} is a scalar function ≤ 0.

As an example of (1) the density can be evaluated by

$$\rho_a = \sum_b m_b W_{ab}, \tag{4}$$

where $W_{ab} = W(\mathbf{r}_a - \mathbf{r}_b, h)$, though in practice it is often an advantage to calculate the density from the continuity equation which, in SPH form, can be written

$$\frac{d\rho_a}{dt} = \sum_b m_b \mathbf{v}_{ab} \cdot \nabla_a W_{ab}, \tag{5}$$

where $\mathbf{v}_{ab} = \mathbf{v_a} - \mathbf{v_b}$. This notation is used for vectors throughout this paper. ∇_a denotes that gradient derivatives are taken with respect to the coordinates of particle a.

In all the simulations presented in this paper we use a cubic kernel constructed from two B-splines requiring that both the kernel and its derivative be continuous. The kernel is

$$W(q, h) = \frac{15}{7\pi} \begin{cases} \frac{2}{3} - q^2 + \frac{1}{2}q^3, & 0 < q < 1 \\ \frac{1}{6}(2 - q)^3, & 1 < q < 2 \ , \\ 0, & \text{otherwise} \end{cases} \tag{6}$$

where $q = \mathbf{r}_{ab}/h$. This is a relatively low-order kernel with around 18 neighbouring particles contributing to the interpolated quantities at each particle location. For many fluid dynamic applications quartic kernels are used with an average of around 28 neighbouring particles contributing. These higher order kernels demonstrate higher accuracy and stability. The results presented here for heat conduction using the lower order cubic kernel are therefore really worst case results which can be improved further by using higher order kernels.

2.1. *The General Energy Equation*

A very general energy equation for fluid flows (eq. 10.1-13 from [1]) is

$$\rho \frac{DU}{Dt} = -\nabla \cdot \mathbf{q} - P(\nabla \cdot \mathbf{v}) - (\tau : \nabla \mathbf{v}), \tag{7}$$

where U is the thermal energy/mass, ρ is the density, P is the pressure, $\mathbf{v}$ is the velocity, and τ is the stress. The terms on the RHS of (6) correspond to conduction, reversible internal energy changes caused by compression, and irreversible losses due to viscous dissipation.

The conductive heat flux is given by

$$\mathbf{q} = -k\nabla T, \tag{8}$$

where T is the temperature and k is the conductivity. k may depend on T and on other material properties. Assuming that the fluid is Newtonian allows the viscous dissipation to be rewritten as Φ_v (see [1, p. 316]). The energy equation then becomes

$$\rho \frac{DU}{Dt} = \nabla \cdot (k\nabla T) - P(\nabla \cdot \mathbf{v}) + \mu \Phi_v. \tag{9}$$

No other simplifying assumptions having been made in the derivation of this equation.

The energy equation can be rewritten in terms of the temperature,

$$\rho c_v \frac{DT}{Dt} = \nabla \cdot (k\nabla T) - T \left(\frac{\partial P}{\partial T} \right)_V (\nabla \cdot \mathbf{v}) + \mu \Phi_v, \tag{10}$$

where V is volume/unit mass and μ is the dynamic viscosity.

If the fluid is ideal then the flow is adiabatic and reversible. The equation of state for an ideal gas is

$$P = \rho RT, \qquad \text{implying} \left(\frac{\partial P}{\partial T} \right)_V = \frac{P}{T}. \tag{11}$$

The energy equation expressed in terms of T then becomes

$$\rho c_v \frac{DT}{Dt} = \nabla \cdot (k\nabla T) - P(\nabla \cdot \mathbf{v}) + \mu \Phi_v. \tag{12}$$

One can use either the internal energy or the temperature as the principal variable for determining the heat flows. If the connection between internal energy and temperature is simple, for example,

$$U = c_v T, \tag{13}$$

then Eq. (12) follows immediately from Eq. (9). If the functional relationship between internal energy and temperature is more complex, as is the case for liquid metals, then the internal energy equation (9) is the more appropriate of the two. For more complex thermodynamic processes, such as those involving phase changes, the enthalpy H is generally a better choice of independent variable with the governing equation being similar to Eq. (9), with H replacing U.

Distributed heat sources and sinks of magnitude ϵ per unit volume can be added to the right-hand sides of either (9) or (12).

For conduction in an incompressible solid the energy equation reduces to

$$\rho\frac{dU}{dt} = \nabla \cdot (k\nabla T). \tag{14}$$

2.2. A Preliminary SPH Conduction Equation and Error Estimates

The simplest way to construct an SPH heat conduction equation would be to start with an interpolated T and form its gradient by exact differentiation, then multiply by k, and then differentiate again to form the divergence. However, the resulting expression is too sensitive to particle disorder to be of practical use. A better approach is to explore integral approximants to the thermal conduction equation. For an ideal gas where $\xi = k/\rho$ we use the integral approximant

$$2\int \rho(\mathbf{r}')\frac{\xi(\mathbf{r}') + \xi(\mathbf{r})}{\rho(\mathbf{r}') + \rho(\mathbf{r})}[T(\mathbf{r}) - T(\mathbf{r}')]G(\mathbf{r} - \mathbf{r}')\,dr', \tag{15}$$

with

$$G(\mathbf{q}) = \frac{\mathbf{q} \cdot \nabla W(\mathbf{q})}{q^2 + \eta^2}, \tag{16}$$

where $\eta = 0.01h$ acts as a clipping constant to prevent singularities when the positions of two particles with different temperatures coincide. Although we have retained this form of G, the spherically symmetric kernel we use allows us to write

$$\nabla W(\mathbf{q}) = \mathbf{q}F(\mathbf{q}), \tag{17}$$

and then we can take $G = F$ with no singularities.

On converting (15) to SPH form we find

$$\frac{1}{\rho}\nabla \cdot (\rho\xi\nabla T) = 2\sum_b m_b \frac{\xi_a + \xi_b}{\rho_a + \rho_b}(T_a - T_b)F_{ab}, \tag{18}$$

where $F_{ab} = F(\mathbf{r}_a - \mathbf{r}_b)$. When k is constant or a function of the temperature we use the integral approximant

$$\frac{1}{\rho(\mathbf{r})}\int[k(\mathbf{r}') + k(\mathbf{r})][T(\mathbf{r}) - T(\mathbf{r}')]G(\mathbf{r} - \mathbf{r}')\,dr', \tag{19}$$

which in SPH form is

$$\frac{1}{\rho}\nabla \cdot (k\nabla T) = \sum_b \frac{m_b}{\rho_a\rho_b}(k_a + k_b)(T_a - T_b)F_{ab}. \tag{20}$$

The SPH form of the heat equation (14) is then

$$\frac{\partial U_a}{\partial t} = \sum_b \frac{m_b}{\rho_a\rho_b}(k_a + k_b)(T_a - T_b)F_{ab}. \tag{21}$$

TABLE I

Coefficient of Conduction Term in PDE for Various Values of $h/\Delta x$
and Different Order Interpolation Kernels

Kernel	1.0	1.2	1.5	1.8	2.0
Cubic	1.0000	1.0224	0.9877	0.9907	1.0000
Quartic	1.0000	0.9967	1.0034	1.0012	1.0000
Gaussian	0.9981	1.0000	1.0000	1.0000	0.9987

This approximation to the heat conduction equation conserves total thermal energy and ensures that the entropy increases.

An estimate of the accuracy of this summation can be made for the case of equispaced particles modelling a homogeneous material in one dimension. After Taylor series expansion of T_b we find

$$\frac{\partial U}{\partial t} = \alpha k \frac{\partial^2 T}{\partial x^2} + \beta \Delta x^2 \frac{\partial^4 T}{\partial x^4} + \cdots. \tag{22}$$

For consistency with the original partial differential equation the coefficient α should be 1. The second term on the right is the lowest order error term which is spatially second order.

The coefficient α and β are given by summations of F_{ab}. Table I gives the values of α for a Gaussian, the cubic kernel (6), and a quartic kernel. The summation for the infinite Gaussian kernel is truncated after five terms of the series expansion. For $h/\Delta x = 1$ both the cubic and the quartic kernels have $\alpha = 1$ and are consistent with the original PDE. For $h/\Delta x = 1.2$ the value of α is slightly higher than unity for the cubic kernel and slightly lower than unity for the quartic one. As $h/\Delta x$ increases $\alpha \to 1$ for both these kernels. This reflects increasing numbers of particles in the summations which approximate the original integrals progressively more exactly. However, as $h/\Delta x$ increases, the computational cost increases, so there is a trade-off between accuracy/consistency and speed. In this paper we choose the worst combination of the cubic kernel and $h/\Delta x = 1.2$ and show that the numerical performance of even this case is very good. The other combinations of kernel and smoothing length are expected to perform even better than this. The error in the coefficient α manifests as a proportional error in the thermal diffusivity. This can complicate efforts to establish the order of the error terms. The coefficient β of the error term for $h/\Delta x = 1.2$ is 0.123, 0.150, and 0.180 for the cubic, quartic, and Gaussian kernels, respectively.

If the integrals are done exactly (meaning that if there are an infinite number of particles in the summations in Eq. (21) then the $O(\Delta x^2)$ and higher order error terms vanish in Eq. (22)) then there are still $O(h^2)$ errors because this integral differs from the actual heat conduction $\nabla \cdot (k \nabla T)$ term by $O(h^2)$ errors. So, as we increase $h/\Delta x$, the summations approximate the integrals better but the error term associated with the original interpolation increases slowly. The situation with disordered particles is even more complicated. The integral interpolant still has the same error $O(h^2)$ but the summation introduces errors which are probably larger than $O(\Delta x^2)$. If we could use arbitrarily many particles we could reduce h more slowly than the particle spacing (even if disordered), and the summation would be very close to the integral and the overall error would be $O(h^2)$.

While it is possible to analytically quantify the errors in terms of particle spacing and kernel for very simple configurations described above (homogeneous properties, equispaced particles, no discontinuities), it is not possible to do so for general configurations, especially when the particles are disordered. We therefore examine the convergence and accuracy of the SPH conduction algorithm by numerical means later in this paper.

2.3. *Discontinuous Thermal Conductivity*

To take into account a discontinuous thermal conductivity we consider the simple problem of heat conduction in one dimension x with thermal conductivity k_l if $x < 0$ and k_r if $x > 0$.

In order to solve this problem the usual procedure is to solve the heat conduction problem separately in each region and require that the heat flux be continuous at the interface between the regions.

If we use finite differences with points spaced by Δx, and denote the temperature at the interface by T^*, the condition that the flux be continuous gives

$$k_l \frac{(T^* - T_j)}{\Delta x/2} = k_r \frac{(T_{j+1} - T^*)}{\Delta x/2}, \tag{23}$$

where point j is the last point on the left of the interface and point $j + 1$ is the first on the right of the interface. We then find

$$T^* = \frac{k_r T_{j+1} + k_l T_j}{k_r + k_l}. \tag{24}$$

To solve the heat conduction equation for the material with $x < 0$ we approximate the conduction equation at the point j by

$$\frac{\partial u_j}{\partial t} = k_L \left(\frac{(T^* - T_j)}{\Delta x/2} - \frac{(T_j - T_{j-1})}{(\Delta x)} \right) \frac{1}{\Delta x}. \tag{25}$$

If we now substitute for T^* we find

$$\frac{\partial u_j}{\partial t} = \left(\frac{2(T_{j+1} - T_j)k_L k_R}{(k_L + k_R)\Delta x} - \frac{k_L(T_j - T_{j-1})}{\Delta x} \right) \frac{1}{\Delta x}. \tag{26}$$

This result shows us that the effect of requiring the flux into the adjoining region to be continuous is equivalent to the first point of that region being included in the heat conduction equation but with the effective thermal conductivity

$$\frac{2k_l k_r}{k_l + k_r}. \tag{27}$$

If we had examined the heat conduction for the material on the right then the effect of the continuity of flux between the regions is to include the point j with the effective thermal conductivity we have just derived. In summary, the heat conduction for either region can be computed using the adjacent point of the adjoining region but with the effective conductivity (27).

A similar argument can be used with the SPH equations. The final result is that (21) becomes

$$\frac{dU_a}{dt} = \sum_b \frac{4m_b}{\rho_a \rho_b} \frac{k_a k_b}{k_a + k_b} T_{ab} F_{ab}. \tag{28}$$

This heat conduction equation is the final one used for numerical tests throughout this paper. It ensures that heat flux is automatically continuous across material interfaces. Multiple materials with substantially different conductivities and specific heats can then be accurately simulated. Although this equation was derived by simple arguments for a configuration where the heat flux was parallel to the vector between adjacent particles, it will be shown by extensive numerical tests in the following sections to be true in general.

3. BOUNDARY PARTICLES, BOUNDARY CONDITIONS, AND HEAT FLUX

All boundaries are modelled by boundary particles. These particles are assigned a mass, position, density, conductivity, and temperature.

In the case of dynamical simulations the boundary particles interact with the fluid particles through boundary forces that prevent the fluid passing through the boundary. The boundary forces are in the direction of the local inward normal which is also used to correctly estimate heat fluxes.

Adiabatic boundaries are simulated by integrating the energy equation for the boundary particles together with those for the interior. Summing (28) over all particles shows that energy is conserved.

The implementation of isothermal boundaries is very simple since we just need to maintain boundary particle temperatures at the specified values. This is straightforward in a particle method. More complex flux based boundary conditions, such as radiative and convective ones, can also be implemented but are beyond the scope of this paper.

The calculation of the thermal flux at the boundary is more difficult because the number of particles falls to zero so that estimates of gradients become less accurate. The problem is exacerbated if the thermal conductivity jumps discontinuously at the boundary.

If the boundary is adiabatic there is no flux through the boundary. If the boundary is isothermal then the flux can be calculated by forming the gradient of the temperature (method A). Alternatively we can use the energy equation to calculate how much heat is transferred to a boundary particle after which the boundary particle temperature is set back to the isothermal value (method B). In either case corrections must be made for the falloff in particle number density at the boundary.

Method A involves evaluating the temperature gradient at each isothermal boundary particle location

$$\Phi_a = -k\mathbf{n} \cdot \nabla T = \frac{1}{\rho_a} \sum_b 2m_b k_b (T_a - T_b) \mathbf{r}_{ab} \cdot \mathbf{n}_a G_{ab}, \tag{29}$$

where $\mathbf{n}_a$ is the unit inward normal for a particle a on an isothermal boundary.

The SPH formulation of gradients assumes that there is at least one particle on either side of a given particle in the direction of the normal. For calculations involving a boundary particle, its neighbours lie on only one side. The effective length used to estimate the

derivative is twice what it should be. The factor 2.0 arises to cancel this and give an approximately correct gradient.

To obtain the flux using method B we start with the heat conduction equation (27),

$$\frac{\partial u_a}{\partial t} = \sum_b \frac{m_b}{\rho_a \rho_b} \frac{4 k_a k_b}{(k_a + k_b)} (T_a - T_b) F_{ab}, \tag{30}$$

from which we deduce that energy added or subtracted from particle a per unit time is

$$\Delta U_a = \sum_b \frac{m_b}{\rho_a \rho_b} \frac{4 k_a k_b}{(k_a + k_b)} (T_a - T_b) F_{ab}. \tag{31}$$

The boundary particles are separated by Δx so that the thermal energy (30) must be considered transferred to (or from) this length of boundary. For the two-dimensional problems we consider in this paper the flow of thermal energy per unit area and per unit time is therefore

$$\frac{m_a}{\Delta x \rho_a} \sum_b \frac{m_b}{\rho_b} \frac{4 k_a k_b}{(k_a + k_b)} (T_a - T_b) F_{ab}. \tag{32}$$

This expression should be a good approximation to $-k\mathbf{n} \cdot \nabla T$ at the boundary particle. This can be checked by expanding $T_a - T_b$ as a Taylor series and keeping the dominant terms. We find [6] that Eq. (31) is a very good approximation to Eq. (27) if the density ρ_a of boundary particle a is

$$\rho_a = -\frac{m_a}{\Delta x} \sum_b \frac{m_b}{\rho_b} \frac{4 k_b}{(k_a + k_b)} \mathbf{r}_{ab} \cdot \mathbf{n}_a F_{ab}. \tag{33}$$

By examining the terms in the summation for one- and two-dimensional configurations in the case where the thermal conductivity is constant we find [6] that the boundary densities required by Eq. (32) are always within 7% of the density of the adjacent fluid.

4. TIME INTEGRATION

The integration technique used in the present version of the SPH code is a improved Euler predictor–corrector method (see [11] for precise details). This is well suited to fluid dynamics problems and is used here because we intend to solve coupled heat and fluid flow problems. If we were intending to solve purely conduction problems then we would have used other schemes allowing longer timesteps. It is a common misconception that particle methods must use explicit time stepping and are limited to small timesteps. In fact, the choice of timestepping scheme is independent of the spatial discretisation, and any other scheme could be implemented in the same way as they would for other continuum methods such as finite differences and finite elements. In particular, implicit solution of the SPH equations is possible and can be done with matrix solvers similar to those used for unstructured finite elements.

At the beginning of a timestep of the predictor–corrector, the existing velocities, densities, thermal energy, and other properties are used to predict new values at the midpoint of the timestep. The rates of change of all these properties are then calculated at this midpoint. These are used to update the properties at the end of the timestep.

The size of the timestep for a pure conduction problem is given by

$$\Delta t = \beta \rho c_v h^2 / k = 1.44 \beta \rho c_v \Delta x^2 / k, \tag{34}$$

where β is a constant, $h = 1.2 \Delta x$ is the SPH smoothing length scale, and Δx is the particle spacing. The timestep is proportional to the timescale for diffusion to occur across the interpolating kernel. The choice of β is limited by stability.

In order to determine an optimal value of β we performed a wide range of test simulations. If $\beta \leq 0.15$ the integration is stable. For the present calculations we take $\beta = 0.1$. Further details can be found in [3].

5. HEAT CONDUCTION IN SLABS

5.1. *Homogeneous Case*

This two-dimensional configuration consists of a finite slab of homogeneous material. The left half is initially cold with $T_l = 0$ and the right half is hot with $T_r = 1$. The slab has unit width (in the direction of the temperature gradient) and various lengths. The material properties are $k = 1$, $c_v = 1$, $\rho = 1000$, giving thermal diffusivities $\alpha_l = \alpha_r = 0.001$. In the following subscripts, l and r refer to properties in the left and right halves, respectively. The particles were set up on a regular $2n_x$ by n_y lattice with equal spacing in each direction. The hot and cold regions are both n_x particles long. The SPH interpolation length h is chosen to be $h = \Delta x$, where Δx is the particle spacing in the x- and y-directions.

The exact solution can be approximated for some time by the solution for an infinite slab with a temperature discontinuity at $x = x_m$ [8]. This is the limiting case as our slab becomes wider. It is a good approximation while the variation in temperature of the outermost points is very small,

$$\frac{T - T_l}{T_c} = \begin{cases} \text{Erfc}((x - x_m)/\alpha_l t) & \text{if } x < x_m \\ 1 + \sqrt{\alpha_l / \alpha_r} \, \text{Erf}((x - x_m)/\alpha_r t) & \text{if } x > x_m \end{cases}, \tag{35}$$

where $T_c = (T_r - T_l)\sqrt{\alpha_l}/(\sqrt{\alpha_r} + \sqrt{\alpha_l})$, x_m is the location of the initial discontinuity in temperature, and $\alpha = k/\rho c_v$ is the thermal diffusivity.

Figure 1 shows the temperature as a function of the distance across the slab at various times using a resolution of $n_x = 40$ along the slab and $n_y = 20$ across the slab. The temperatures of all the SPH particles are drawn as dots. In general, each visible dot actually represents n_y particles. Any vertical dispersion of the dots corresponds to variations of T with y and represents errors in the SPH solution. The exact solution is shown by the solid curve. The L_2 error in T is 0.29% at $t = 0.1$ and declines to 0.12% at $t = 1.0$ s. These errors are small even at this modest resolution. This is very important for large-scale industrial coupled heat and fluid flow solutions.

Examining Fig. 1a, we find some differences between the exact and SPH temperature for a few positions very close to the discontinuity. The relative weights of the dots indicate that only a couple of points have the higher errors. These maximum errors are around 3–4% and are produced by edge effects at the horizontal adiabatic sides. Essentially, the edge effects in the summations cause the heat transfer along the adiabatic edges to be marginally slower than that through the center of the material. It should be noted that these peak errors
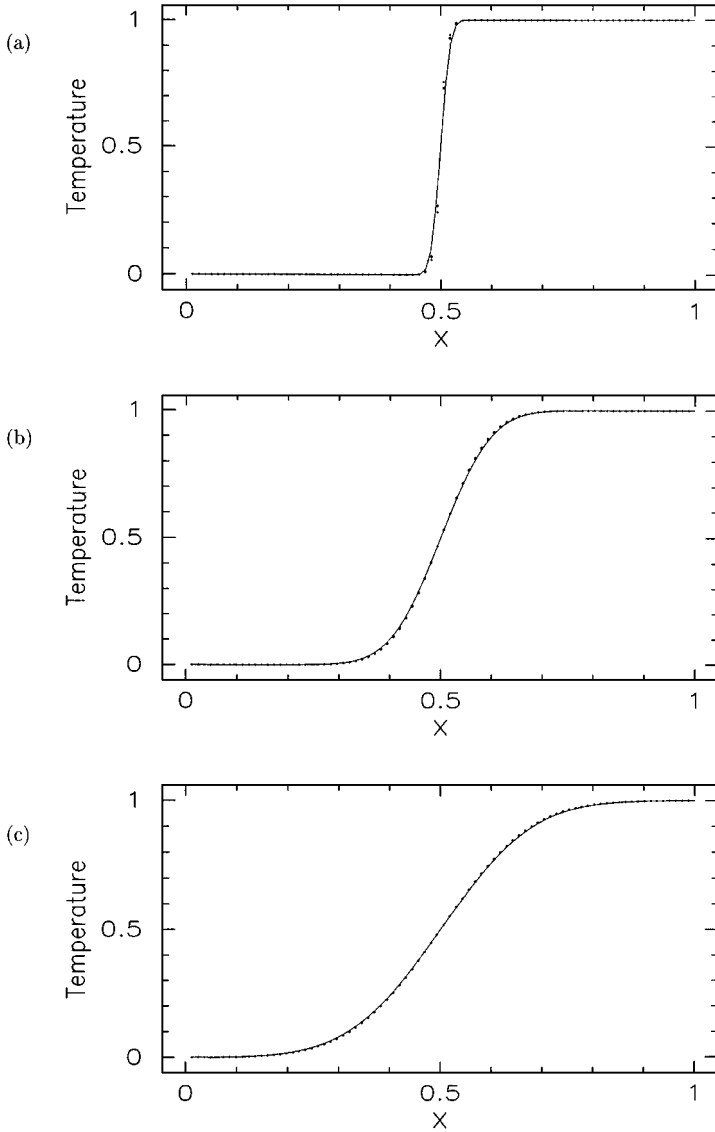
FIG. 1. Temperature profile across a slab at times (a) $t = 0.07$, (b) $t = 4$, and (c) $t = 10$. The exact solution is given by the solid line, whilst the SPH solution is shown as dots.

for a few-edge particle are an order of magnitude larger than for the remainder of the interior particles, including those within the region of high-temperature gradient. This will be discussed in more detail later. This small y dependence of the solution always decays quickly and is not detectable by $t = 1$.

Figure 1b shows the SPH and exact solutions midway through the simulation. They compare very well. This is typical of the accuracy throughout the simulation. The difference is largest near the center because the heat transfer along the adiabatic top and bottom is marginally slower than that through the middle of the slab.

By $t = 650$ the temperature profile has become almost uniform. At the left and $T = 0.4990$ and at the right end $T = 0.5010$. These differences represent 0.2% variations from the
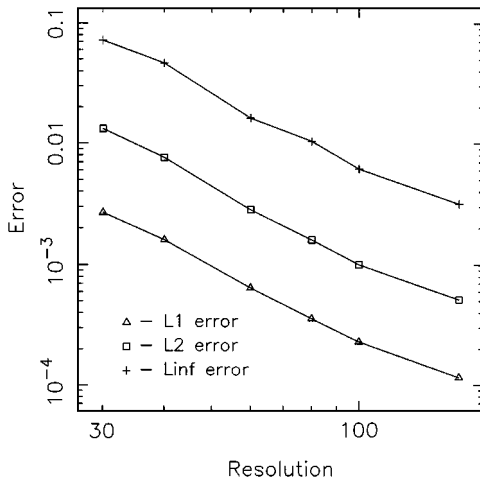
FIG. 2. L_1, L_2, and L_∞ errors at $t = 0.1$ s for conduction in an infinite material with resolutions n_x from 30 to 120. This demonstrates that the SPH spatial resolution for conduction is second order.

average temperature $T_c = 0.5$. The differences are symmetric and have an error of 0.01%. This demonstrates that the heat content of the slab is conserved to very high accuracy.

5.2. *Spatial Accuracy and Convergence*

To rigorously examine the spatial accuracy of the SPH conduction solution we calculate L_1, L_2, and L_∞ norms of the pointwise error of the SPH solution from the exact solution. The configuration used is similar to the one just described but has periodic boundaries in the y-direction. This eliminates the effects of boundary conditions. The solution is effectively for an infinite material with an initial temperature discontinuity.

The largest errors occur early in the simulation after a few rows of particles have entered the high-temperature gradient region, but before the discontinuity has been smoothed out much by conduction. We therefore choose to evaluate the worst case errors at $t = 0.1$ s. The temperature profile at this time is very close to the one shown in Fig. 1a.

Figure 2 shows the errors for spatial resolutions from 30 to 120. Resolutions below 30 do not give meaningful errors at $t = 0.1$. This occurs because the timestep of the explicit integration is either larger than or comparable to this time interval and several timesteps are required for the errors to grow to their largest levels. For resolutions of 30 and higher these conditions are met and the errors can be compared.

The L_1 errors are the smallest (as one would expect), with the L_2 errors being consistently five times higher and the L_∞ errors a further factor of six times higher. Each of the three error curves is essentially linear with least squares slopes of -1.934, -1.997, and -1.934, respectively. The demonstrates both the convergence of the SPH solution towards the exact one and that the SPH spatial discretisation is second order accurate.

We repeat the same tests for the original configuration shows in Fig. 1 (a block of material 1 m wide and 0.5 m high with an array of $2n_x \times n_x$ particles and adiabatic top and bottom edges) in order to evaluate the effect of the adiabatic boundaries on accuracy and convergence.

Figure 3 shows the three error measures for resolutions between 30 and 120. All three curves are again essentially linear. In absolute terms the L_1 and L_2 errors are slightly
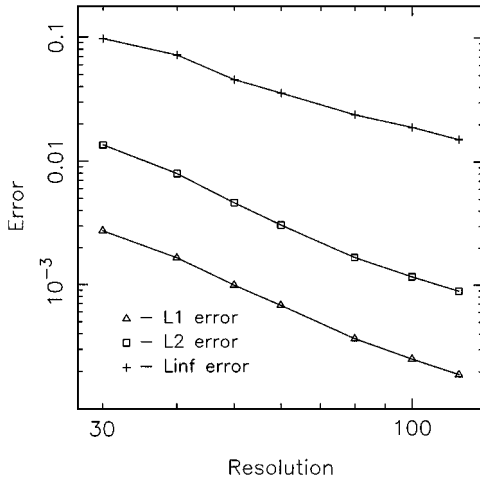
FIG. 3. L_1, L_2, and L_∞ errors at $t = 0.1$ s for conduction in an finite slab of material with adiabatic sides for resolutions n_x from 30 to 120.

higher than for the periodic boundary case, reflecting the modest larger contributions of the adiabatic edge particles. The gradients of these two lines are -1.975 and -2.018, respectively, indicating that the inclusion of adiabatic boundaries does not reduce the second order accuracy of the solution. The L_∞ errors are produced entirely by the adiabatic particles. Increasing the resolution in the y-direction does not affect these errors at all. The L_∞ line has a gradient of -1.376, indicating that the increasing resolution in the x-direction improves the errors for these edge particles by an amount that is closer to first order in space than to second. It is important to realise that the effect of these adiabatic boundary particles decreases with increasing resolution in y, so although the L_∞ error measure is not second order, the L_1 and L_2 measures are.

5.3. Discontinuous k

This configuration is similar to the previous one, but the slab of unit width is now periodic in the y-direction. For this test problem there are two different materials touching along the discontinuity at $x_m = 0.5$. The material on the right half of the slab has a lower conductivity. Otherwise their material properties are the same. Initially, the material on the left is at $T_l = 0$ and the material on the right is at $T_r = 1$. In all subcases $k_r = 1$ whilst k_l is varied from 10 to 1000.

Figure 4a shows the temperature profile for $k_l = 10$ and $t = 1$ using a resolution $n_x = 40$. At $t = 0.05$ there is a small difference between the SPH and the exact solution. By $t = 0.2$ the two solutions are very close and by $t = 1$ they are almost indistinguishable. The SPH solution fully captures both the shape of the temperature profile and its evolution.

The maximum L_∞ error in the temperature of the material on the left is 9.8% at the first timestep. This error occurs at the discontinuity and declines rapidly below 1% (by $t = 0.15$). The material on the right has a lower thermal conductivity and so adjusts more slowly to changes in the material on the left. This means that the errors are higher in the less conductive material and take longer to decline. The L_∞ error for the temperature on the right peaks at 5.5% $t = 0.032$ and then drops off quickly, but not as rapidly as the the error for the left material. The L_2 errors decline with time from 0.3 to 0.1%. Overall these
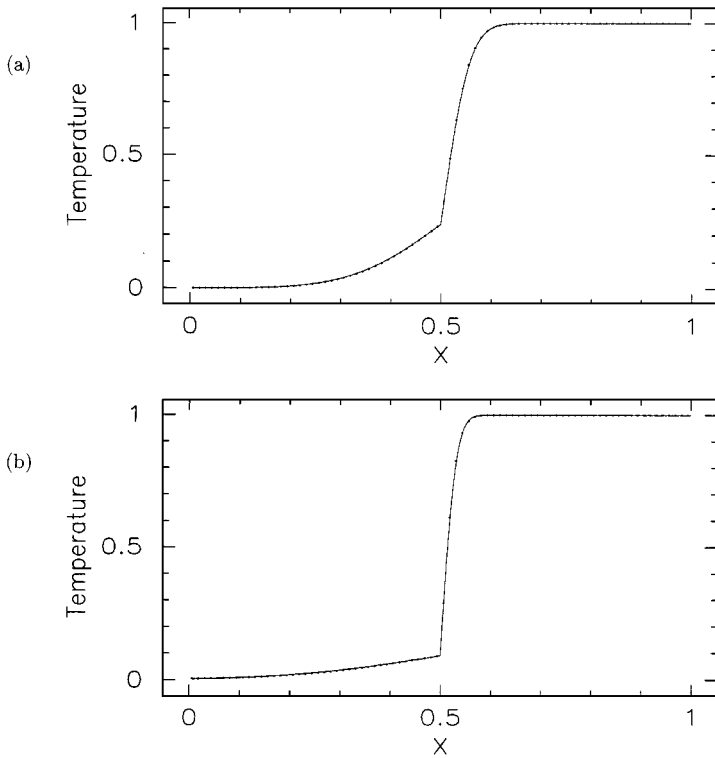
FIG. 4. The temperature across the slab for (a) $k_l = 10$ at time $t = 1$ and (b) $k_l = 100$ at $t = 0.2$. The exact solution is given by the line and the SPH temperatures by the dots.

errors are comparable to those found for the homogeneous case at the same times and resolution. The L_2 and L_∞ errors are slightly higher for the less conductive material than for the homogeneous material, whilst the errors for the more conductive material are lower than for the homogeneous case.

At $t = 337$, the slab is almost at a uniform temperature of $T = 0.5$. The temperature of the leftmost particle is $T = 0.49828$ and that of the rightmost particle $T = 0.50489$. The average of these differs from the correct average by 0.32%. This is also a measure of the overall conservation of heat. The result, although very good, is less accurate than that obtained for the homogeneous slab.

Figure 4b shows the temperature profile when $k_l = 100$ and $t = 0.2$. At the very earliest times the SPH temperature profile for the material on the left has a small but noticeable separation from the exact solution. This difference decays quickly. By $t = 0.1$ the separation has become very small and the two solutions are very similar. The SPH and exact solutions are indistinguishable after $t = 0.3$. The L_2 error has a maximum of 0.35% at $t = 0.05$ s and less than 0.1% at $t > 0.3$ s.

5.4. Discontinuous k, ρ, and c

The setup for this test problem is again similar to the previous cases. The two materials on either side of the slab now both have the same thermal diffusivity, but different values of k, ρ, and c. We choose $k_l = c_l = 1$ and $\alpha_l = \alpha_r = 0.001$ and test the effect of conduction between materials with different conductivities and heat capacities.
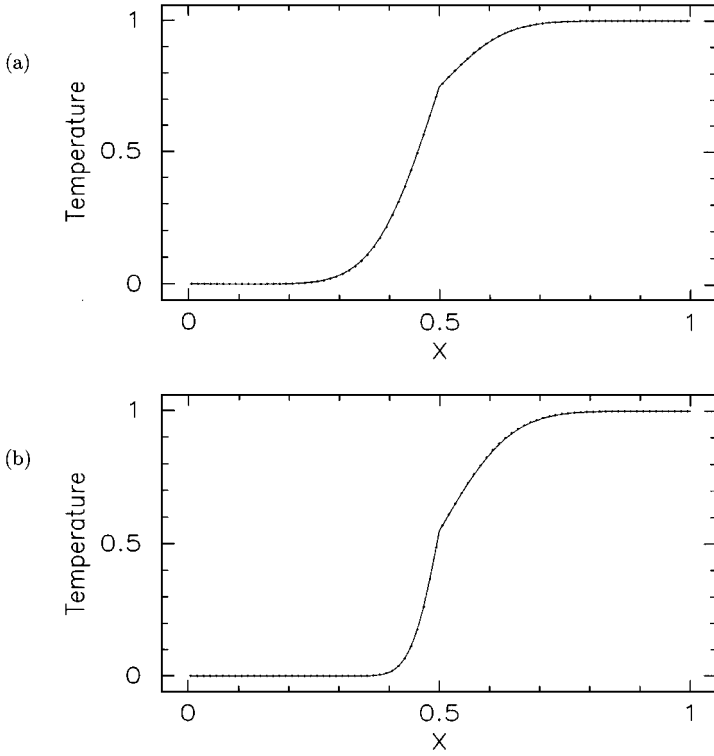
FIG. 5. The temperature across the slab for (a) $k_r = c_r = 3$ at $t = 5$ and (b) $k_r = 3$ and $\rho_l = 2000$ at $t = 2$. The exact solution is given by the curve and the SPH temperatures by the dots.

The exact solution for an infinite slab with a temperature discontinuity at $x = x_m$ for this more general case is

$$\frac{T - T_l}{T_c} = \begin{cases} \text{Erfc}((x - x_m)/\alpha_l t) & \text{if } x < x_m \\ 1 + (k_l/k_r)\sqrt{\alpha_r/\alpha_l} \, \text{Erf}((x - x_m)/\alpha_r t) & \text{if } x > x_m \end{cases}, \tag{36}$$

where $T_c = (T_r - T_l)(k_r/\sqrt{\alpha_r})/(k_r/\sqrt{\alpha_r} + k_l/\sqrt{\alpha_l})$, x_m is the location of the the discontinuity.

Comparing the SPH and the exact solution when $k_r = c_r = 3$, we find at the very early stages that there is only a small difference in the region of the initial temperature discontinuity. By $t = 0.2$ the two solutions are very close together and by $t = 1$ they are almost indistinguishable. Figure 5a shows the temperature profile for this case at $t = 5$. The SPH solution fully captures both the shape of the temperature profile and its evolution.

The errors in the temperature for the material on the left are around three times greater than those for the material on the right. This is in line with the ratios of the conductivities and specific heats. As usual they peak at the beginning of the simulation when the temperature gradient at the interface is greatest. By $t = 1$ the errors are less than 1%. Again, the initial errors decay quickly, leaving the solution highly accurate.

At $t = 500$ the temperature of the rightmost particles is $T = 0.7510$ and that of the leftmost particles $T = 0.7474$. The average of these is $T = 0.7492$. This is very close to the

theoretical equilibrium temperature of $T = 0.75$ that arises from the higher heat capacity of the material on the right. The conservation of heat is accurate to 0.016%.

Figure 5b shows the SPH and exact solutions for $k_1 = c_l = 1$ and $\rho_l = 2000$ for the left material, and $k_r = 3$, $c_l = 1$ and $\rho_l = 1000$ for the right material. As before, the SPH solution is highly accurate.

Ratios of thermal diffusivity up to 1000:1 were tested and demonstrate similar accuracy. Of particular interest is the case with air ($k_1 = 0.0254$, $c_l = 1.012$, and $\rho_l = 1.226$—the left material) and water (at 300 K) ($k_r = 0.620$, $c_r = 4.179$, and $\rho_r = 1000$—the right material). The SPH solution and the exact solution are shown in Fig. 6 for three times in the early and middle stages of the evolution. The SPH solution is remarkably accurate, even
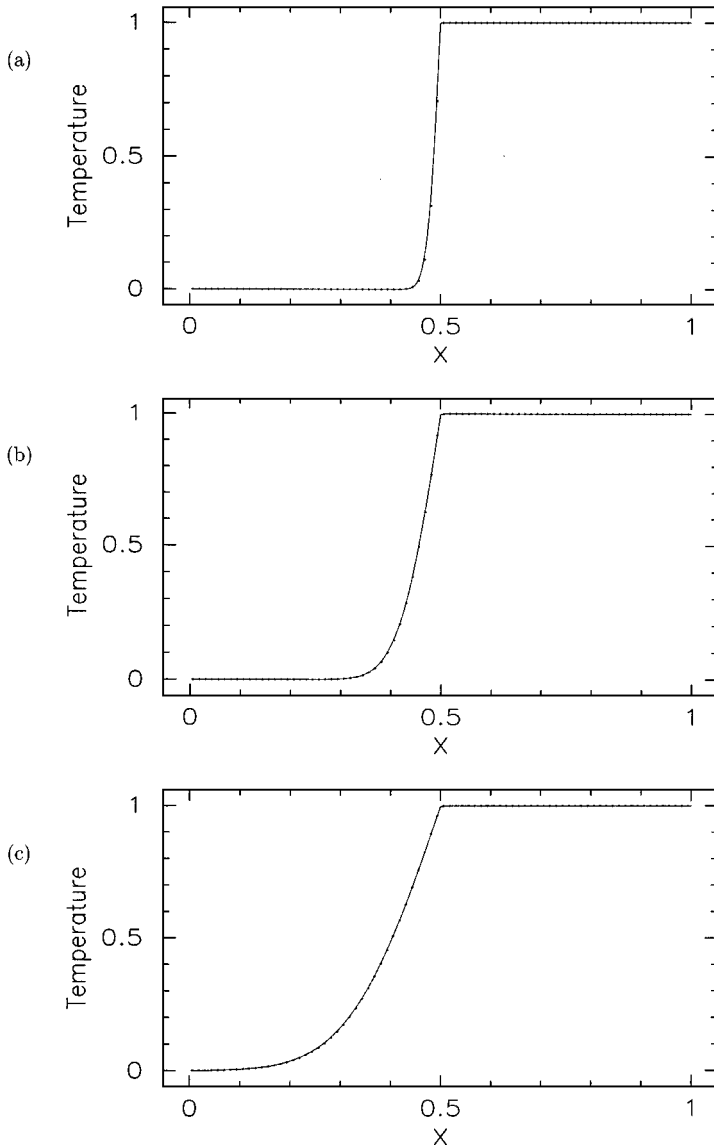
FIG. 6. Temperature profiles for conduction between air on the left and water on the right at times (a) $t = 0.01$, (b) $t = 0.1$, and (c) $t = 0.5$.

at $t = 0.01$, despite the very large differences in the material properties, particularly the density.

6. CONDUCTION IN A SLAB WITH ISOTHERMAL ENDS

6.1. *Homogeneous*

In the previous examples the edges of the materials have been either adiabatic or periodic. Here we explore the use of isothermal boundary conditions. The configuration consists of a homogeneous slab of unit width in the x-direction and periodic in the y-direction. The left edge is maintained at temperature $T_l = 0$ and the right edge is maintained at $T_r = 1$. The material on the left of the centerline $x < x_m$ is initially at T_l and the material on the right is initially at T_r. The material properties are $k_l = c_l = k_r = c_r = 1$ and $\rho_l = \rho_r = 1000$. Both sides have the same thermal diffusivity $\alpha_l = \alpha_r = 0.001$.

Figure 7 shows the asymptotic temperature profile. It is almost exactly linear. The exact linear asymptotic profile is shown as the solid line. The L_2 and L_∞ error norms are 0.03 and 0.15%, respectively, for $n_x = 40$. This demonstrates that the isothermal boundary formulation described earlier gives accurate results even for modest spatial resolution.

Examining the behaviour of the errors with the spatial resolution (shown in Fig. 8), we find that the introduction of the isothermal boundary particles reduces the SPH conduction solution to first order. This can be understood by examining the Taylor series expansions of Eq. (28). The first order terms normally vanish because of symmetry arguments about the balancing odd order contributions of particles to either side. If there is an isothermal boundary then there are no particles on one side and the cancellation ceases, leaving first order error terms. Using the isothermal boundaries in conjunction with the boundary density corrections given in Eq. (33), however, improves the spatial errors to order 3/2. This occurs because of improvements to the normalisation of the kernels near the boundaries produced by the increased density of these boundary particles.

6.2. *Inhomogeneous k*

For this case the material properties are the same as before except now $k_l = 10$. Initially the temperature is described by the error function solution in Eq. (34) and the temperature of the interface is $1/(1 + \sqrt{10}) \approx 0.24025$. As the isothermal boundaries begin to add and
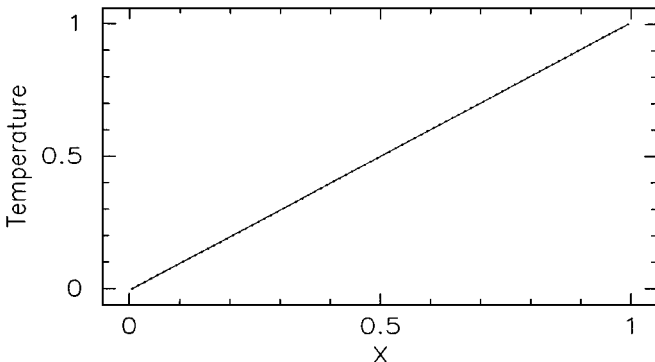
FIG. 7. The asymptotic temperature profile (at $t = 135$) is very close to the linear exact solution when hot and cold isothermal boundary conditions are applied to the sides of the slab.
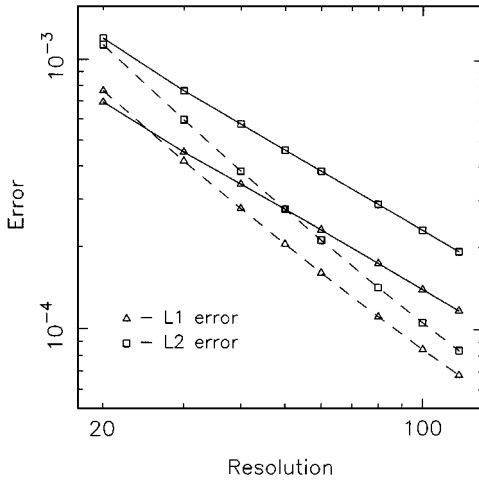
FIG. 8. L_1 and L_2 errors at $t = 135$ s for steady conduction in a homogeneous block with isothermal ends (in x) for different resolutions n_x from 20 to 120. The solid lines are the errors when no boundary density corrections are used, whilst the dashed lines show the improvement in the order of accuracy when the boundary density corrections are used.

remove heat, the temperature profiles straighten and the temperature of the interface tends asymptotically towards

$$T_i = \frac{k_r}{k_l}(T_r - T_l) = \frac{1}{10}. \tag{37}$$

The asymptotic temperature profile (at $t = 135$) shown in Fig. 9 is piecewise linear and matches the exact solution closely. The temperature at the interface is correctly predicted. The maximum difference between the SPH and the piecewise linear exact solution at $t = 135$ is 0.29% for the less conductive material and 0.59% for the more conductive material. The L_1 error is 0.24%. The error is, as usual, larger for the more conductive material, but is still small even for modest resolutions.

This demonstrates that isothermal boundary conditions can be easily implemented in SPH by simply not changing the temperature or internal energy of the isothermal particles boundary particles and that the solutions have satisfactory accuracy.
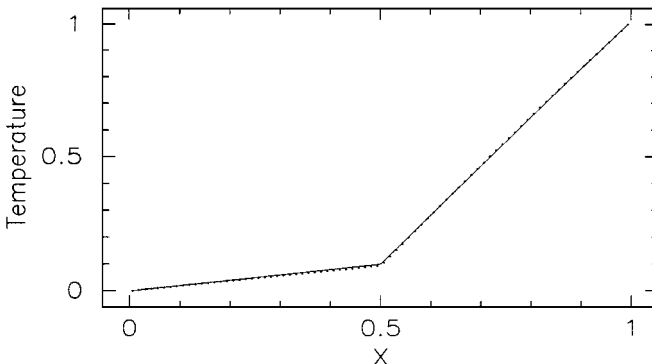
FIG. 9. The steady temperature profile for a slab with isothermal sides (at $T_l = 0$ and $T_r = 1$) and a material discontinuity at $x = x_m$. The material on the left has $k = 10$ and the one on the right has $k = 1$.

6.3. *Temperature-Dependent Conductivity*

Next we examine the accuracy of solutions when the conductivity varies with the temperature. This is common when there are large temperature ranges and particularly in industrial applications.

As before, we use a semi-infinite slab of unit width with isothermal sides (one heated $T_r = 1$ and one cooled $T_l = 0$). The initial temperature is $T = 0$ in the left half and $T = 1$ in the right half. The conductivity varies as

$$k(T) = e^{\kappa T}, \tag{38}$$

where κ is a constant.

Since analytic transient solutions are not available for this problem, we use *Fastflo* (a finite element package [9]) to generate an alternative numerical solution with which to compare. The *Fastflo* solution uses fully implicit timestepping and is spatially second order accurate with 40 quadratic elements across the width of the slab. The 80 nodes across the width of the slab gives the same spatial resolution as the 80 SPH particles used.

Figure 10 shows a sequence of snapshots of the temperature profile for both the SPH (dots) and FEM (line) methods for $\kappa = 4$. This represents a factor of 54 variation in conductivity across the width of the slab. There are small differences between the solutions at each time, but overall they track each other (both spatially and temporally) very closely. The FEM solution is slightly more diffusive than the SPH solution. Figure 10c shows the two solutions near the asymptotic limits. The FEM approaches the limit a bit more slowly than the SPH solution. The timesteps used here are $\Delta t = 0.00412$ for *Fastflo* and $\Delta t = 0.000412$ for SPH (given by the limit in Eq. (34)). The L_1 norm of the difference between the SPH and *Fastflo* solutions is 0.11% and the L_∞ difference is about 1%. The relative error contributions of the FEM and the SPH are unquantifiable. Importantly, the two solutions are very close in both time and space. This level of accuracy at modest resolution is important for practical applications involving fluid flow.

The exact solution for the the steady-state temperature profile, when $k = e^{\kappa T}$, is given by

$$T = \frac{1}{\kappa} \ln \left(\frac{(e^{\kappa} - 1)}{(1 - 2\delta)}(x - \delta) + 1 \right), \tag{39}$$

where $\delta = \frac{1}{2}\Delta x$ is the position of the first SPH particle (where the boundary condition $T = 0$ is applied) and $x = 1 - \delta$ is the position of the last particle (where the $T = 1$ boundary condition is applied).

Figure 11 compares the asymptotic temperature profiles for the SPH solutions with the analytic steady-state solutions, for a range of κ. In each case the SPH solution is very close to the FEM solution, even when the temperature gradient adjacent to the cold isothermal boundary becomes very steep. This demonstrates that the use of the harmonic average conductivity in the SPH heat equation (28) to ensure flux conservation when there are rapid changes in conductivity gives suitably accurate solutions.

The heat flux through either isothermal boundary, once the heat flow has reached equilibrium, is

$$\Phi = \frac{1}{\kappa}(e^{\kappa} - 1). \tag{40}$$

Figure 12 shows the heat fluxes through both the left and the right boundaries. The solid curves are the SPH heat fluxes calculated using method B and the dashed lines show the
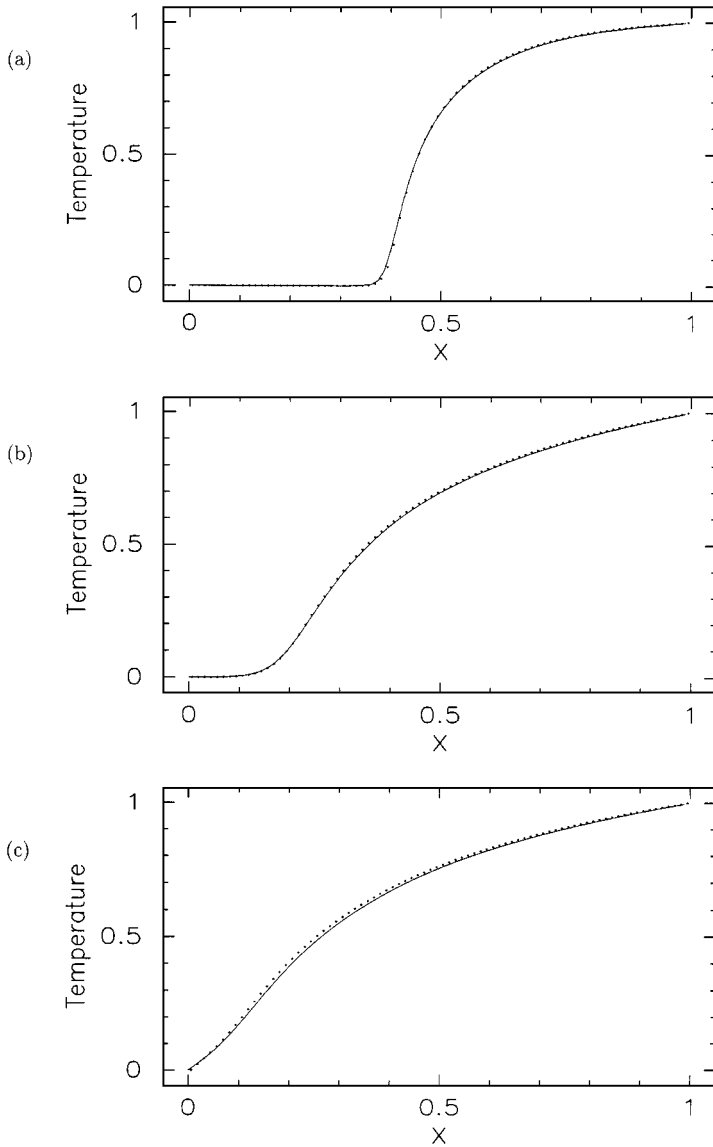
FIG. 10. The temperature profiles produced by a temperature-dependent conductivity with $\kappa = 4$ at (a) $t = 0.6$, (b) $t = 5.0$, and (c) $t = 10$. The SPH temperatures are given by the points and the *Fastflo* temperature is given by the curve.

fluxes using Method A (see Section 3). The horizontal dot–dash line is the exact asymptotic limit for the fluxes (from Eq. (40) with $\kappa = 4$). The dotted curves are the fluxes calculated using *Fastflo* (which we expect to be highly accurate because of the use of 80 finite elements across the block). For each of the SPH and *Fastflo* solutions there are two curves. The upper ones show the hot wall heat fluxes. They rise rapidly and overshoot the asymptotic limit and then drop back asymptotically towards the limit (38). The lower curves show the cold wall heat fluxes. They remain zero until around $t = 9$. This reflects the time taken for the front of the heated region to propagate through the comparatively less conductive material. Once the front reaches the cold boundary the flux rises rapidly, as the conductivity of the
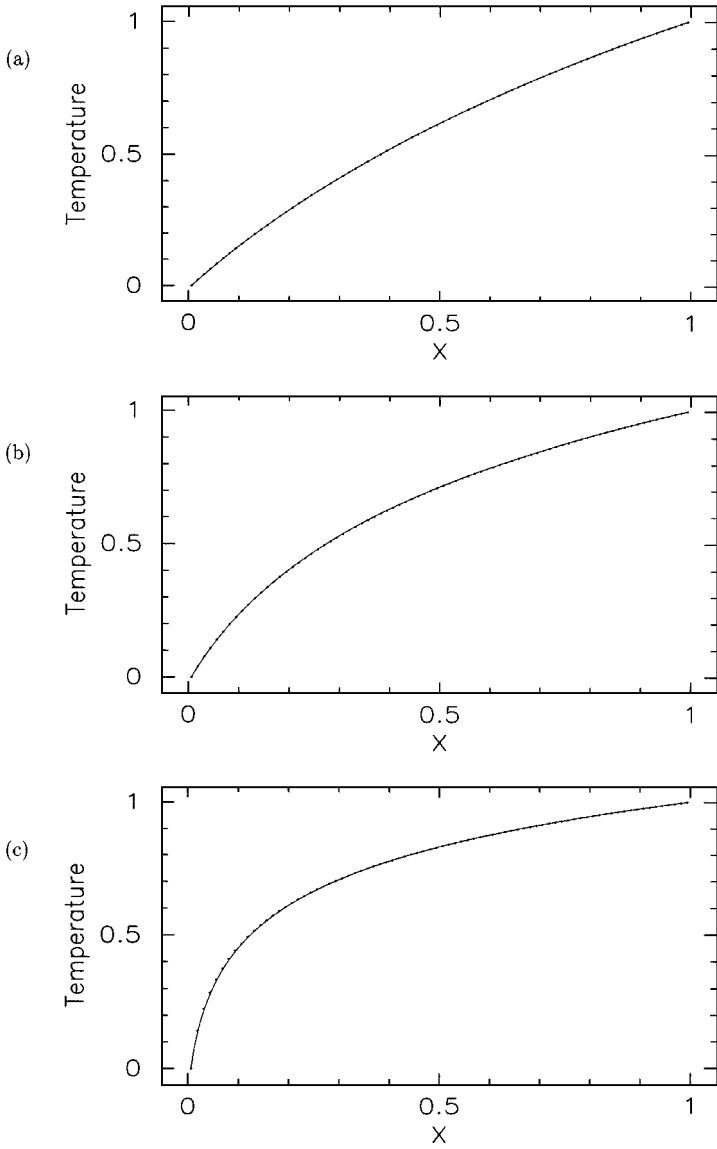
FIG. 11. Asymptotic temperature profiles with an exponentially temperature-dependent conductivity for (a) $\kappa = 1$, (b) $\kappa = 2$, and (c) $\kappa = 4$. The exact solution is shown as the curve and the SPH solution as the points.
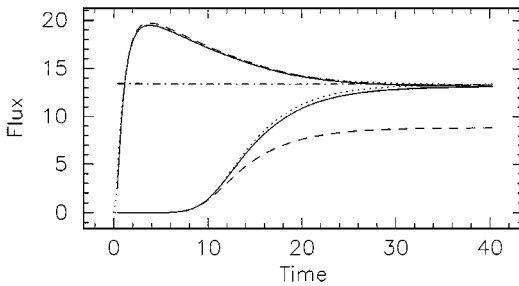
FIG. 12. Heat fluxes through the edges of the slab when the conductivity is an exponential function of temperature and $\kappa = 4$. The corrected densities are only calculated at $t = 0$ and periodic boundaries are used in the vertical direction.

material rises exponentially. The flux then also asymptotes to the limit value as the system approaches thermal equilibrium. An important aspect of this flow is the strong asymmetry of the heat fluxes due to the net heating of the material as the conductivity increases. This indicates that the original amount of heat stored in the slab is much less than the amount stored at equilibrium.

All the heat fluxes for the hot wall (upper curves) are close at all times, with method B being particularly close to that of the accurate *Fastflo* solution. The flux using method B for cold wall (lower curves) is also very close to the *Fastflo* flux. There is only a modest differ-ence as they approach the asymptotic steady limit. The *Fastflo* asymptotic limit differs from the exact value by only 0.03%. The SPH solution by method B (with only 40 particles across the slab) is in error by 1.6%. This is quite acceptable for this resolution. This configuration is a very strong test of the heat conduction because around 10% of the entire temperature difference occurs between the boundary particle and the first interior particle. Method A gives a good representation of the evolution and the final value of the hot wall flux (where the temperature variation is small) but is very poor for the cold wall (where the temperature variation is large). This occurs because this flux uses an explicit estimate of the temperature gradient (given in Eq. (29)) and this gradient uses only the conductivity k_b, not a harmonic mean of k_a and k_b. This demonstrates that method B is a much more robust technique for calculating the heat fluxes. It is also simpler to implement and computationally faster.

If the boundary densities are corrected at each timestep to take account of the time varia-tions of the conductivity near the cold wall, then the cold wall flux diverges further from the *Fastflo* flux and the error in the asymptotic limit increases to 4.0%. This is not surprising, since Eq. (33), used to calculate the corrected densities, assumed that the variations in con-ductivity adjacent to the isothermal boundary were small. For cases where the conductivity change is large, using the initial corrected densities without the conductivity variation seems to yield the best result. The corrected densities are then given by

$$\rho_a = -\frac{m_a}{\Delta x} \sum_b \frac{2m_b}{\rho_b} \mathbf{r}_{ab} \cdot \mathbf{n}_a F_{ab}. \tag{41}$$

Even when the conductivity variation is exponential (with power 4) and the resolution is modest, method B gives good results for the fluxes, their evolution, and their asymptotic values. This gives us confidence that the modest conductivity variations found in industrial applications will not cause problems or any significant errors.

6.4. *Sinusoidal Temperature Variation in x*

This configuration consists of the usual block of homogeneous material with isother-mal sides and adiabatic top and bottom boundaries. The material properties used were $k = 1$, $c_v = 1$, and $\rho = 10$. The density corrections were used along the isothermal bound-aries. The unit normals on the left and right boundaries are chosen to be $\mathbf{n}_l = (1, 0)$ and $\mathbf{n}_r = (-1, 0)$, respectively. These apply even at the corners where there is a discontinuity in the thermal boundary condition. If the normals at the corners are chosen to be directed inwards at $45°$ then there is more variation in the calculated fluxes. The initial temperature distribution is chosen as

$$T(x, y, t = 0) = \sin \frac{\pi x'}{l}, \tag{42}$$
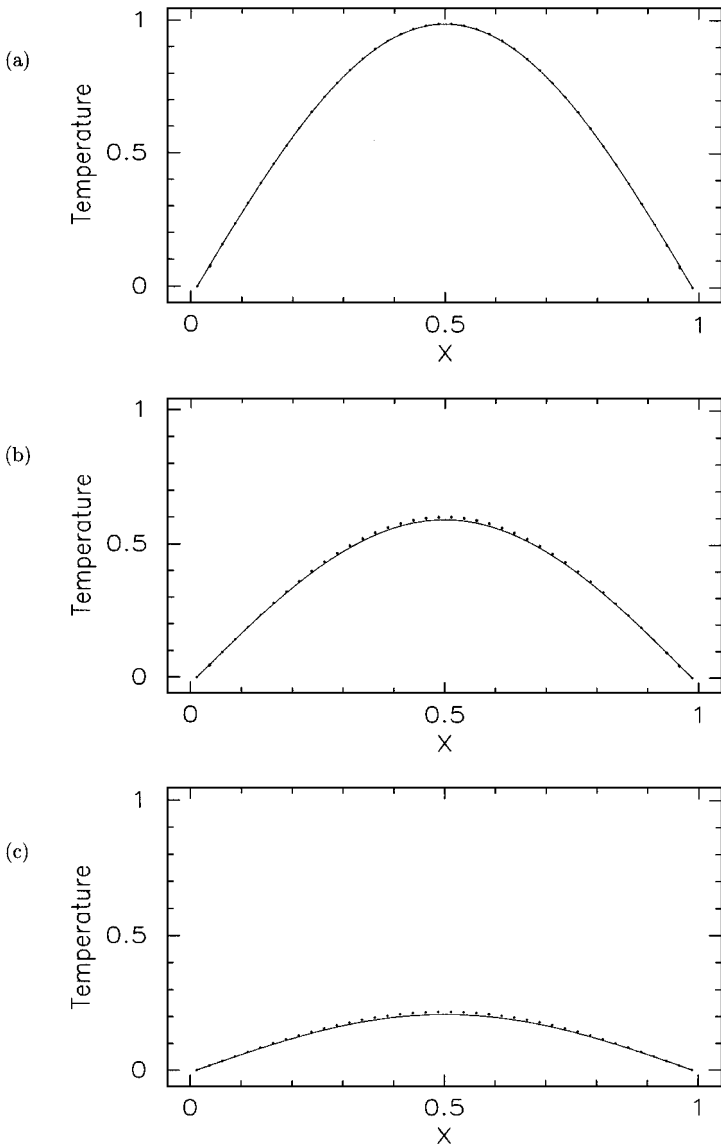
FIG. 13. Sinusoidal temperature profiles across a slab of unit width. The points indicate the SPH temperatures, whilst the curve shows the corresponding exact solution at each time (a) $t = 0.02$, (b) $t = 0.5$, and (c) $t = 1.5$.

where $l = 1 - 2\delta$ is the side length of the block, $x' = x - \delta$, and $\delta = \frac{1}{2}\Delta x$. The exact solution for heat conduction with this geometry and set of initial conditions is

$$T(x, y, t) = \sin \frac{\pi x'}{l} e^{-(\pi/l)^2 \alpha t}. \tag{43}$$

A 40×40 array of SPH particles was used. Figure 13 shows the temperature field at three different times. There is clearly close correspondence between the exact and SPH solutions. The SPH solution predicts both the form of the profile and its evolution.

Figure 14 shows the exact and SPH values of the average fluxes absorbed by the isothermal sides as functions of time, (a) with and (b) without the density correction. The solid line
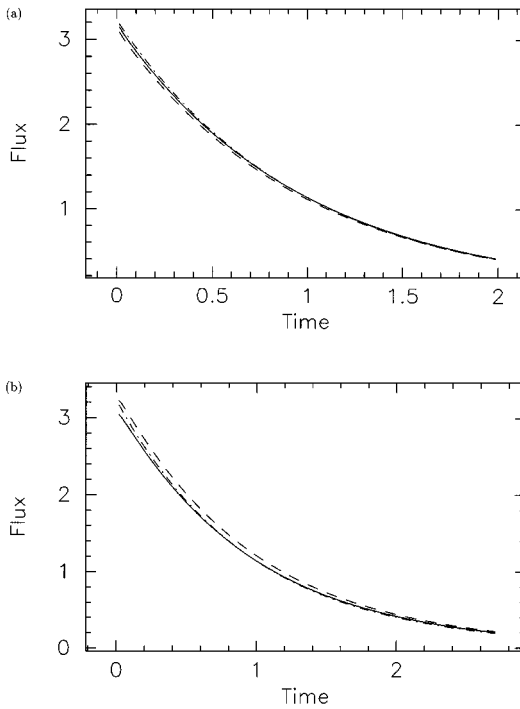
FIG. 14. Evolution of the SPH and exact average fluxes through the isothermal boundaries of a slab with a sinusoidal temperature profile, using the (a) corrected boundary densities and (b) uncorrected densities.

corresponds to method B and the dashed line corresponds to method A. The exact value of the flux is shown as the dot–dash line and is given by

$$\Phi(y, t) = k\mathbf{n} \cdot \nabla T = ke^{-(\pi/l)^2}\alpha t. \tag{44}$$

The fluxes (with corrections) shown in Fig. 14a match the exact solution very closely with Method B being more accurate. When the corrected densities are not used (Fig. 14b) the accuracy of the fluxes deteriorates, with the deterioration being larger for method A. In this case the error changes from a slight underestimation to an overestimation and its magnitude doubles. The most accurate method is method B using the density correction.

The errors (measured relative to the maximum flux at that time) are largest at the corners. The error in the corners quickly rises to around 8%, then slowly decreases to 4.5% at $t = 2$. By comparison the error in the flux across the large uniform central region begins at 0.6% and slowly declines. At $t = 0.52$ it becomes slightly larger than the exact flux. This difference slowly increases to around 2% by $t = 2$.

The important conclusion here is that the majority of the error in the flux is contributed near the corners at which the adiabatic and isothermal boundaries intersect. The end effects extend about four particle spacings from the corners. Since the interpolation is a multiple of the particle spacing, increasing resolution will not affect the number of boundary particles with these corner errors, but will decrease their relative contribution to the overall error. For this case the resulting average flux remains accurate to around 1% throughout the simulation.

6.5. *Sinusoidal Temperature Variation in x and y*

In this case the temperature is a function of x and y, and all the boundaries of the square block are isothermal. The principal complication arises from the existence of corners. The block consists of an $n_x \times n_x$ array of particles placed on a grid with the first row and column at $y = \delta = \Delta x/2$ and $x = \delta$, respectively. The initial temperature distribution is given by

$$T(x, y, t = 0) = \sin\frac{\pi x'}{l} \sin\frac{\pi y'}{l}, \tag{45}$$

where $l = 1 - 2\delta$ is the side length of the block, and $x' = x - \delta$ and $y' = y - \delta$. The temperature along all four isothermal edges is $T = 0$.

The exact solution for conduction in this geometry with this set of initial conditions is

$$T(x, y, t) = \sin\frac{\pi x'}{l} \sin\frac{\pi y'}{l} e^{-2(\pi/l)^2 \alpha t}. \tag{46}$$

The material properties used here are $k = 1$, $c_v = 1.5$, and $\rho = 10$ and the resolution is $n_x = 40$. Figure 15 shows a sequence of temperature distributions. The temperature is shown as a function of x. Since there is a line of particles for each of the n_x values of y and the temperature distribution is symmetric (with respect to reflection in the x- and y-directions through the middle of the block) there are $n_x/2 + 1$ distinct curves in each frame. These correspond to temperatures along different horizontal slices of the block (parallel to the x-axis). The SPH temperatures are shown as points and the exact solution for each value of y is shown as a curve. The SPH solutions are clearly very close to the exact ones. The spatial distributions of temperature in both the x- and y-directions are highly accurate (average relative error $\ll 1\%$). Their temporal evolution is also extremely accurate.

The symmetry of the problem means that the heat flux through each side is identical. The flux through the boundary $x = \delta$ or $x = 1 - \delta$ is

$$\Phi(y, t) = k\mathbf{n} \cdot \nabla T = \frac{\pi k}{l} \sin\frac{\pi y'}{l} e^{-2(\pi/l)^2 \alpha t}, \tag{47}$$

Figure 16 shows the evolution of the boundary flux profiles. The SPH fluxes (using method B) are shown as points and the exact fluxes (Eq. (47)) are given by the curve. The fluxes along the top and bottom boundaries of the slab ($y = \delta$ and $1 - \delta$) are shown by the solid curves and matching points. The vertical points at $x = \delta$ and $x = 1 - \delta$ correspond to the SPH fluxes for the sides of the block. Figure 16 shows the behaviour of the boundary fluxes throughout the evolution. The SPH fluxes are very close to the corresponding exact flux curve at each time. The largest discrepancy occurs at the end points (1.57%). The SPH solution clearly predicts spatial distribution of the fluxes with high accuracy. The evolution of the spatial distribution is also accurate.

Integrating the flux along the boundary gives an average heat transfer rate (a dimensional version of the Nusselt number). For this case the average flux is

$$\Phi_{av} = \frac{2k}{l_f} e^{-2(\pi/l)^2 \alpha t}. \tag{48}$$

Here l_f is the length of the boundary used in the SPH flux calculations. This is not the same as the length l used in the temperature calculations. Each SPH particle represents a small square block of material with side length Δx. The distance between the end particles (the
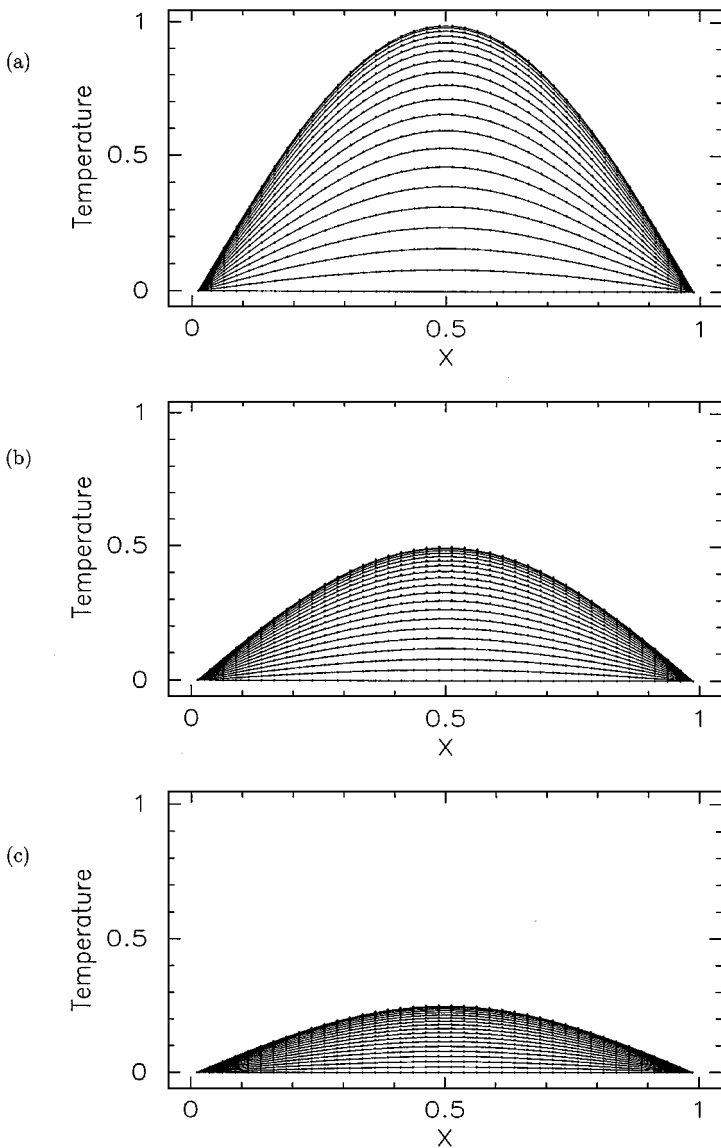
FIG. 15. The temperature profiles for each y-coordinate of the SPH particle lattice showing the various cross sections of the two-dimensional sinusoidal temperature distribution. The points show the SPH temperature of each particle, whilst the curves show the corresponding exact solution at times (a) $t = 0.02$, (b) $t = 0.51$, and (c) $t = 1.01$.

centers of these blocks) is $(n_x - 1)\Delta x$, whereas the length of the real edge (over which the fluxes are calculated) is $n_x \Delta x$, so $l_f = l + \Delta x$. An extra $0.5\Delta x$ is contributed by the parts of each of the end blocks which protrude beyond the centers of the end particles. The evolution of the SPH and exact average fluxes are shown in Fig. 17. The SPH fluxes are calculated by both methods A and B for all four edges. The SPH and exact fluxes are all indistinguishable.

A series of tests were run to determine the dependence of the errors on h, Δx, and the material properties. With $1 \leq h/\Delta x \leq 1.8$ the errors in the maximum flux increase from
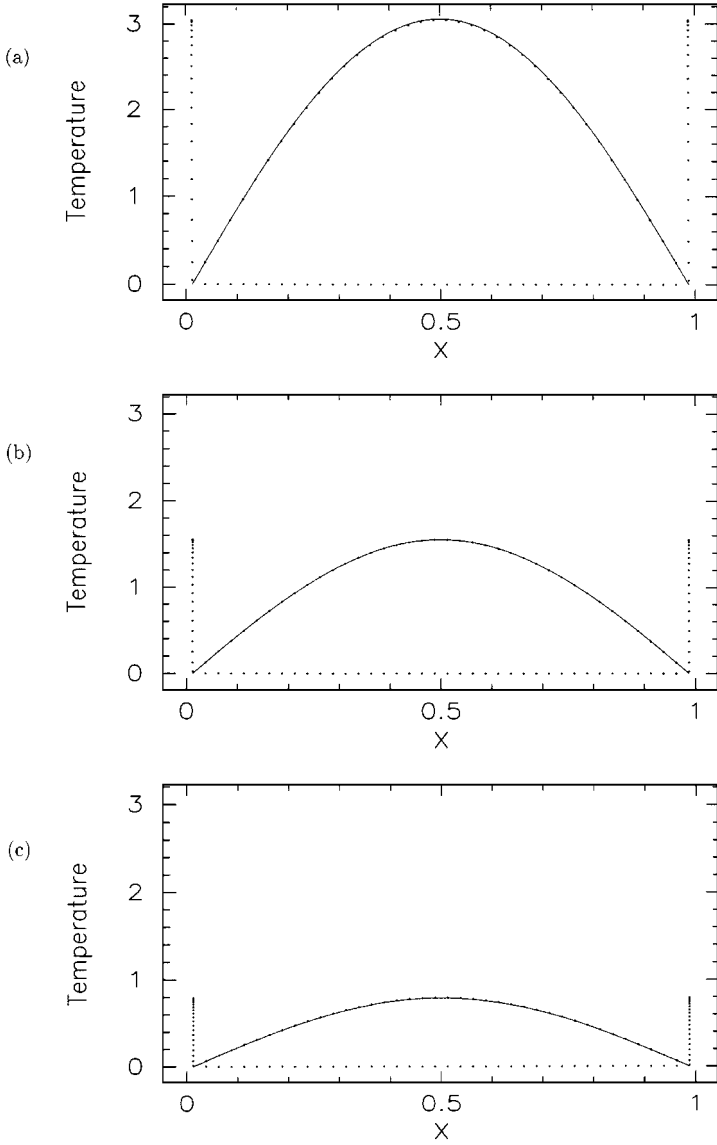
FIG. 16. The heat fluxes through the horizontal isothermal boundaries are shown. The curve is the exact heat flux and the points are the SPH fluxes; (a) $t = 0.0$, (b) $t = 0.5$, and (c) $t = 1.0$.
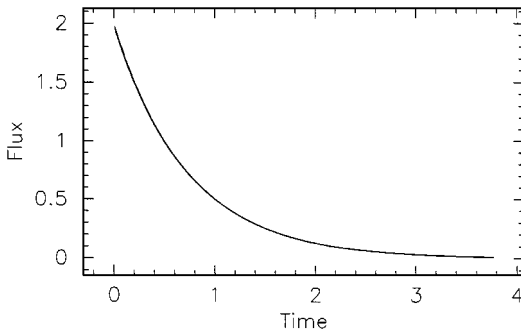
FIG. 17. Evolution of the SPH and exact average fluxes through the isothermal boundaries.

1 to 2.3% as $h/\Delta x$ increases. This means that $h = \Delta x$ is optimal for heat conduction. Decreasing Δx results in lower flux errors as expected. If Δx is reduced by a factor 4, the maximum error is reduced by a factor 10. Further reduction in Δx does not give significant improvement in the maximum error for this problem if $h/\Delta x$ is constant. Our analysis (partly described in Section 2.2) suggests that h must decrease more slowly than Δx to get the correct limit as $\Delta x \to 0$. We have not explored this limit here. The errors in the SPH fluxes were found to be completely insensitive to changes in k, p, and c_v by factors of 100, 6, and 1000, respectively.

7. HOW TO SET UP BOUNDARIES

In previous tests, the edges of the particle lattice were aligned with the edge of the slab. In general this is not the case. So how should we construct the boundaries in such cases? Consider heat conduction in a disc. The naive setup is to take all the particles on a lattice that lie within the bounding circle and to tag the outermost ones as isothermal boundary particles. Such an approach actually produces very poor results. An unphysical temperature discontinuity forms just inside the isothermal particles as the boundary behaves partially isothermally and partially adiabatically. The problem is caused by the uneven spacing of the boundary particles. Nearby interior particles can effectively "see" through the gaps between the isothermal boundary particles and behave partially adiabatically. The local boundary behaviour then depends on the precise details of the particle locations. This is exaggerated by the somewhat erratic directions of the boundary normals.

We have devised simple rules for setting up isothermal boundaries. These rules are consistent with the requirements to set up physical boundaries for fluid flow:

- Boundaries should be set up separately from the interior particles unless they align with the particle lattice.
- Boundary particles should be placed upon smoothly varying curves and should be equally spaced using the interior particle spacing Δx.
- The boundary normals should actually be perpendicular to the underlying boundary curve leading to smooth variations in the orientations of the normals.
- Interior particles within $\sim \frac{1}{3}\Delta x$ of the boundary should be omitted.

7.1. Conduction in a Disc

To demonstrate the importance of setting up the boundary correctly and to show the accuracy that can be obtained using the rules described above we model radial heat conduction in a disc with initial temperature distribution given by the Bessel function
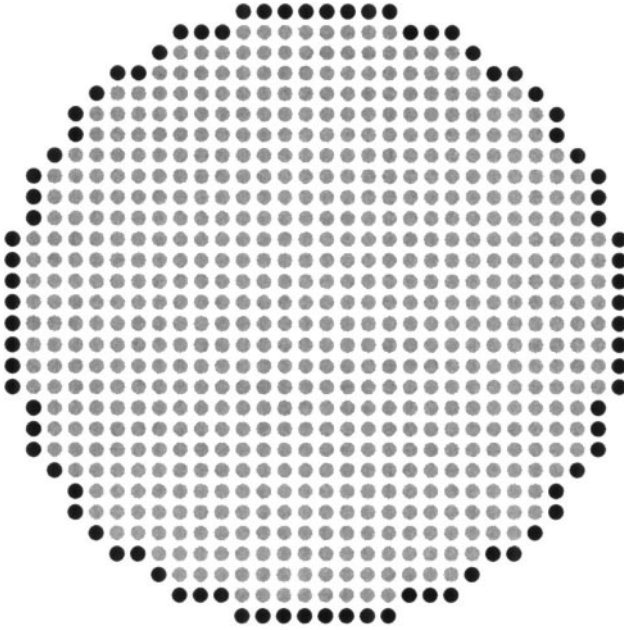
$$T(r, \theta, t = 0) = J_0(\beta_1 r/a), \tag{49}$$

where $\beta_1 = 2.4048$ is the first root of the Bessel function $J_0(r)$. The temperature along the isothermal boundary of the disc is $T = 0$.

The exact solution for heat conduction with this geometry and initial conditions (from [8]) is

$$T(r, \theta, t) = J_0(\beta_1 r/a)\, e^{-\alpha(\beta/a)^2 t}. \tag{50}$$

These simulations use $k = 1.0$, $c_v = 1.0$, and $\rho = 1000$ and $n_x = 30$.
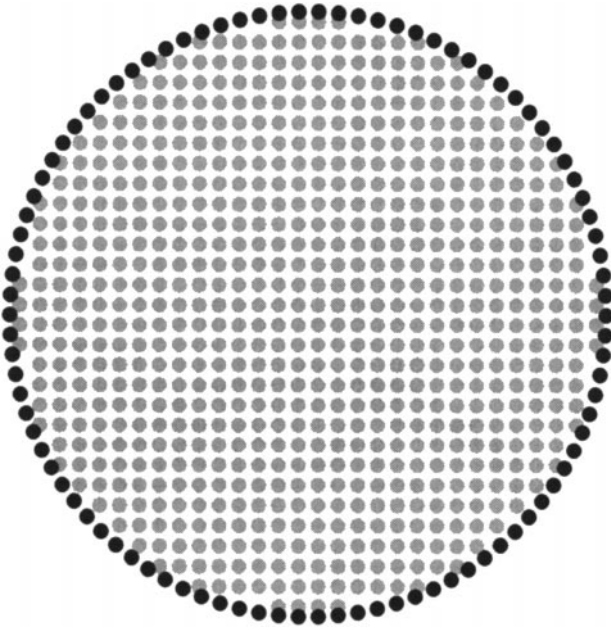
FIG. 18. Particle positions for heat conduction in a disc. The black particles are the isothermal boundary particles.

7.1.1. The naive setup.   The most obvious choice of configuration for modelling heat conduction in a disc of radius a with an isothermal outer boundary involves setting up the particles on a grid and choosing the outermost particles to be the boundary. Figure 18 shows the initial setup. The normals are chosen to be radial. The isothermal particles are chosen to be all those within $\delta s = 0.8\Delta x$ of the outer radius of the disc a, where Δx is the particle spacing. The effective radius of the disc is chosen to be the radial distance of the closest isothermal particle to the center of the disc; increasing δs increases the thickness of the isothermal region and decreases the effective radius of the disc.

Figure 19 shows the temperature profiles for this problem. The SPH particles appear as points and the exact solution (Eq. (50)) is given by the solid line. These results are
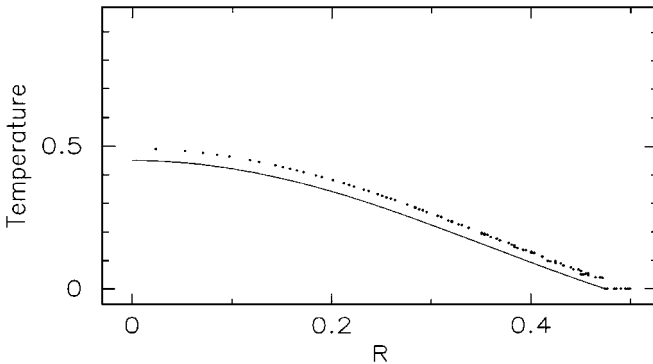
FIG. 19. Radial temperature profile for naive setup at $t = 30.7$. Note the discontinuity in the temperature between the boundary and isothermal particles.

FIG. 20. Particle positions for heat conduction in a disc. The black particles are the isothermal boundary particles and are placed on a circle of radius $a = 0.5$.

very poor. A discontinuity quickly arises in the temperature at the edge of the isothermal boundary. The temperature is uniformly overpredicted. This indicates that the heat transfer to the boundary is too small. The initial height of the discontinuity is about 7% of the peak temperature. At $t = 128$ the average error is 14.6% and the maximum error is 28%. The discontinuity indicates that large sections of the boundary are acting as an insulator rather than as a conductor or heat bath/sink. This result may at first be surprising, but can be understood when it is recognised that the average spacing of the particles is around $1.2\Delta x$. The additional 20% spacing between the isothermal particles means that the outermost internal particles are partially exposed and act as adiabatic boundary particles even though they appear to be inside the disk. This is a result of the SPH method smoothing the effects of particles over distances of $2h$. This demonstrates that this method of construction of isothermal boundaries is inappropriate.

7.1.2. A better setup. An alternative way of setting up the particles is shown in Fig. 20. Here the boundary is constructed as a circle of equally spaced particles with separation very close to that of the interior particle separation Δx. The interior particles are placed on a grid. Particles within $a - \epsilon \Delta x$, where $0 < \epsilon < 1$, of the disc center are included. This configuration has the significant advantages that the boundary is smooth, the normals are really normal to the surface at each point, and the boundary particle spacing is correct. It has the disadvantage that there are some interior points very close to the boundary particles. One question to be answered for this configuration is, How close should the interior particles be to the boundary (that is, what value of ϵ is best) in order to ensure adequate thermal contact between the interior and the boundary? Here we choose $\epsilon = 0.4$.

Figure 21 shows the temperature profiles for this configuration at the same time as for the naive setup shown in Fig. 19. The SPH temperatures are now extremely close to the
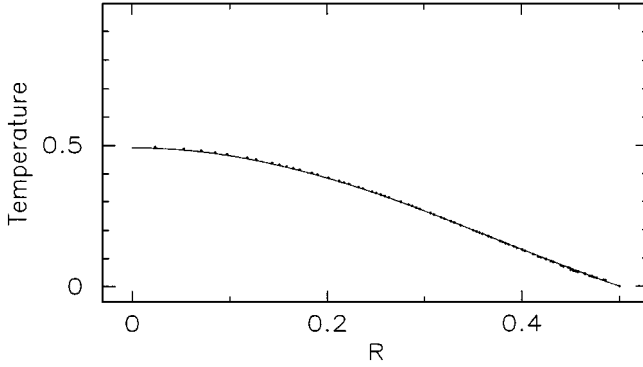
FIG. 21. Radial temperature profile for conduction in a disc with a circular isothermal boundary setup according to our rules at $t = 30.7$.

exponentially declining Bessel function exact solution. The SPH solution has a high degree of radial symmetry and shows little variation from the exact values near the outer boundary. This indicates that for $\epsilon = 0.4$ the thermal contact between the boundary and the interior is satisfactory and that the uneven spacing of the interior particle with respect to the boundary particles does not affect the accuracy of the solution. This is very encouraging for cases where the interior particles are disordered (as in a liquid). The L_∞ errors in the temperature (relative to the maximum temperature at that time) begin at 1% and increase to 1.5% at $t = 128$, while the L_1 errors begin at 0.2% and rise to 0.46%. This is a satisfactory level of error for this small resolution ($n_x = 30$). For $n_x > 30$ the error does not decrease rapidly. We are uncertain of the reason for this but the irregular particle separation from the boundary is likely to be a significant contributor.

The exact flux through the circular isothermal boundary is

$$\Phi(t) = k\beta_1 J_1(\beta_1) e^{-\alpha(\beta_1/a)^2 t}, \tag{51}$$

where $J_1(r)$ is a Bessel function of first order. The heat fluxes are very accurately calculated by both methods when the isothermal boundary is set up in the manner described above. The maximum error for method A is 1.3% and that for method B is 1.7%. For higher resolution $n_x = 50$ the maximum error in the flux calculated by method B reduces to 0.23%, while the method A error increases to 3.9%. This again demonstrates the higher accuracy of method B. Note that the boundary density corrections formulated earlier have been used in this simulation without alteration. If they are omitted, the temperature profile and the flux (calculated with method B) remain largely unchanged.

For very small values of ϵ the temperatures are overpredicted very close to the boundary. This causes a small increase in the error. For values of ϵ larger than 0.42 there is an abrupt decrease in accuracy. This is caused by a sharp drop in the corrected densities from the previous range to 0.61 to 1.1 times the base density. The average boundary density is 25% lower. This means that the thermal connection between the interior and the boundary is much weaker and the heat flux absorbed by the boundary is smaller. This causes the temperature to be overpredicted, especially closer to the center. The flux calculated by method B for $\epsilon = 0.8$ is initially 7% too high, but improves quickly to be only 1–2% in error. For method A, however, the error is 29%. This is a consistent error and unacceptable error throughout the evolution. This behaviour is characteristic of all the cases for $\epsilon > 0.42$.

Simulations for other values of h, for example $h = 1.1\Delta x$ and $1.3\Delta x$, are less sensitive to ϵ. For the 1.1 case, there is a mild decrease in accuracy to around 1.3 from 0.8% when increasing ϵ beyond 0.42. For the 1.3 case values of ϵ as high as 0.8 give quite good results. Since $h = 1.2\Delta x$ is our preferred choice of interpolation length (for reasons described earlier) some care should be taken with choosing ϵ. Values in the range 0.2–0.4 seem to be optimal. The results are insensitive to the choice within this range.

Summarising, the temperature profiles, the fluxes, and their evolutions are all accurate to about 1% when 30 or more particles are used across the disk, the boundary is set up according to our rules, and the corrected boundary densities are used. Both methods of flux calculation then give very good results.

7.2. Conduction Not Aligned with the Particle Lattice

In all the previous slab examples the direction of conduction was aligned with the particle lattice. It is important that there be no deterioration in accuracy when the conduction is across the lattice. We choose the worst case example by rotating a slab by 45° while retaining the particles on the x–y grid. The boundary particles are set up according to the rules devised above and are not part of the interior lattice. This ensures that there are no gaps through which they can "see" outside the block.

The initial temperature field is the same as used earlier (Section 6.4) but rotated by 45°. The material properties are $k = 1$, $c_v = 1$, and $\rho = 1000$. The particle configuration is shown in Fig. 22. The particle spacing in the interior is the same as in the previous calculation ($n_x = 40$) when the particle lattice was aligned with the conduction direction. The boundary particles are spaced according to the rules discussed previously.

Figure 23 shows the temperature field using this configuration. The SPH and exact solutions are very close. The L_1 errors in the temperature using the packed boundary begin at 0.12% and rise to 1.4% at $t = 90$. The L_∞ errors (in the middle of the block) begin at 0.43% and rise to 3.6% at $t = 90$. These errors are calculated relative to the maximum temperature at each time so as usual, a constant absolute error rises as proportion of the declining maximum temperature. These errors are very similar to the results for the non inclined slab.

The alternative "naive" way of setting up the boundary by taking the particles on the original lattice that are within the inclined slab shape produces a sparse boundary. The errors in the temperature then increase substantially with the L_1 error rising to 5.5% and the L_∞ errors to 8.7% (both at $t = 90$). The sparse boundary has effectively four times the errors of the dense boundary (set up according to our rules). This again demonstrates the importance of constructing isothermal boundaries according to our rules.

Figure 24 shows the fluxes (with the usual meaning for the different lines) for the dense and sparse packing of the isothermal boundaries. The flux predictions for the dense boundary (see Fig. 24a) are very close to the exact flux. The fluxes calculated by method B are particularly good with accuracy around 1–2%. This is very acceptable for a resolution of only 29×29. Conversely, the flux predictions for the sparse boundary configuration are extremely poor. The errors of up to 25% for this case again highlight the importance of appropriate setup for the boundary particles and their normals.

Conduction in an annulus was also tested. As a general rule, conduction around the inner hole for which the hole is larger than 10 particle diameters and through solids that are at least 10 particles thick is well resolved and accurate to better than 1% for both the temperature
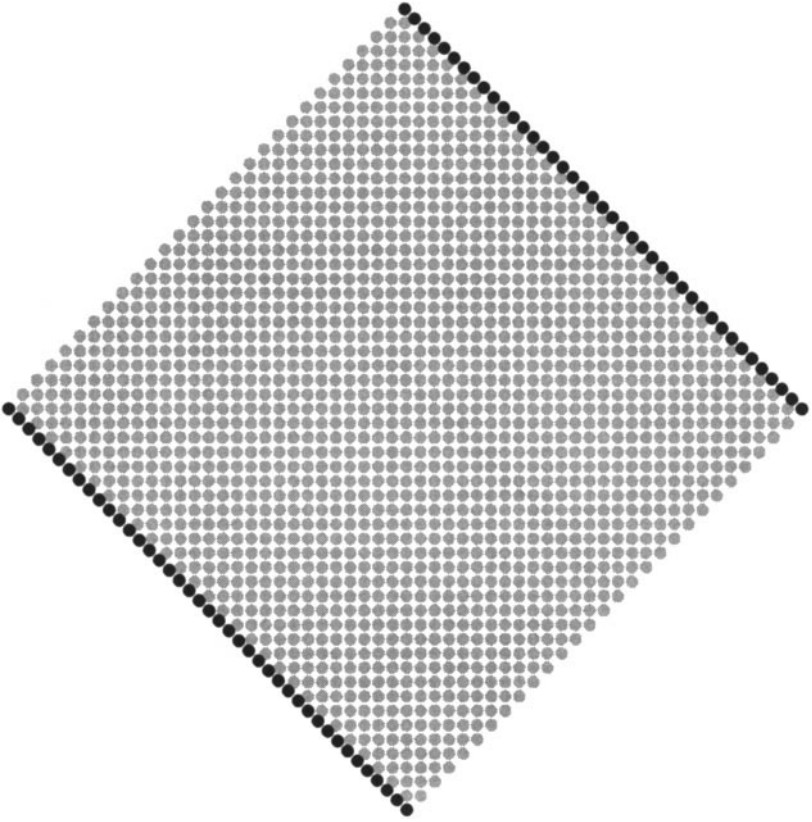
FIG. 22. Particles used to model conduction in an inclined slab with the packed boundary set up according to the rules devised in the text.

profiles and the isothermal boundary fluxes. If the hole is smaller than 10 particles in width, then a higher resolution will be needed in order to ensure the accuracy of the calculation. A minimum number of 10 particles continually recurs throughout this work on conduction. A minimum of 10 particles are needed to resolve conduction properly, regardless of the nature of the complications to the heat flow.
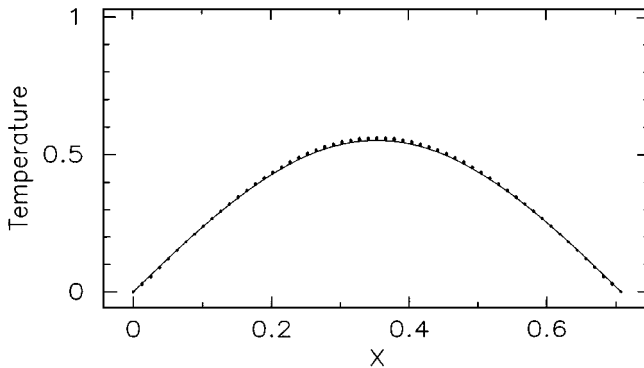
FIG. 23. The temperature across the inclined slab (along the $45°$ centerline) at $t = 50$. The points indicate the SPH temperatures, whilst the curve shows the corresponding exact solution.
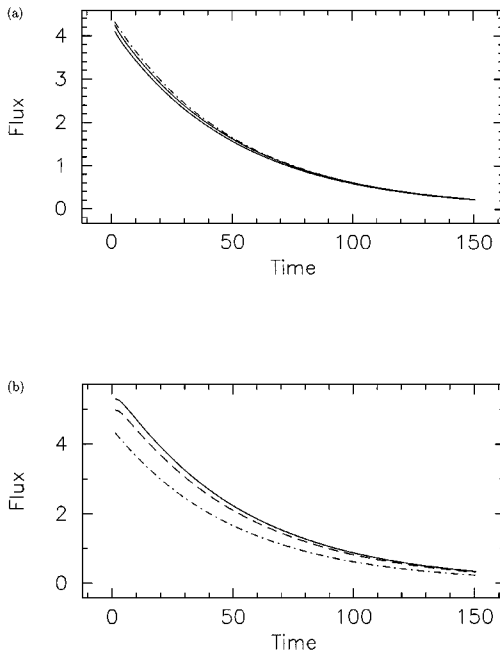
FIG. 24. Evolution of the SPH and exact average fluxes through the isothermal boundaries of the inclined slab, (a) using the packed packed boundary resulting from the rules described in the text and (b) using the sparse boundary produced by selecting boundary from the lattice.

8. CONDUCTION FOR DISORDERED PARTICLES

The accuracy of the solutions of the heat equation was examined for the case where the particles are disordered. This is a particularly important case, since the particle positions usually become disordered whenever a fluid is being modelled.

It is not appropriate to choose random positions for the particles, since these are not indicative of the positions that the particles will occupy during fluid flow simulations. We set up the particle locations in the following way. An initial $n_x \times n_y$ lattice of particles is chosen. The outermost particles are fixed to form a box. The inner particles are allowed to move as a fluid. The SPH equations governing this motion can be found in [11, 12]. The fluid (with viscosity parameter $\alpha = 0.01$) rearranges itself into a standard disordered SPH particle structure. Gravity is turned off so that the pressure throughout the slightly compressible fluid equalises and the fluid maintains equal contact with the top boundary as it has with the bottom boundary. For this part the fluid is made very viscous $\alpha = 0.1$ so that the pressure and density fluctuations begin to damp out. A third step with $\alpha = 1$ damps out all remaining disturbances. The fluid particles are then fixed in space and the required initial temperature distribution and thermal boundary conditions are applied. This produces the initial state for the simulations. A typical example is shown in Fig. 25.

We model conduction in a homogeneous square block with a sinusoidal temperature profile. This test problem is then the same as the one in Section 6.4 except that the interior particles are now disordered. The density corrections are again used along the isothermal boundaries.
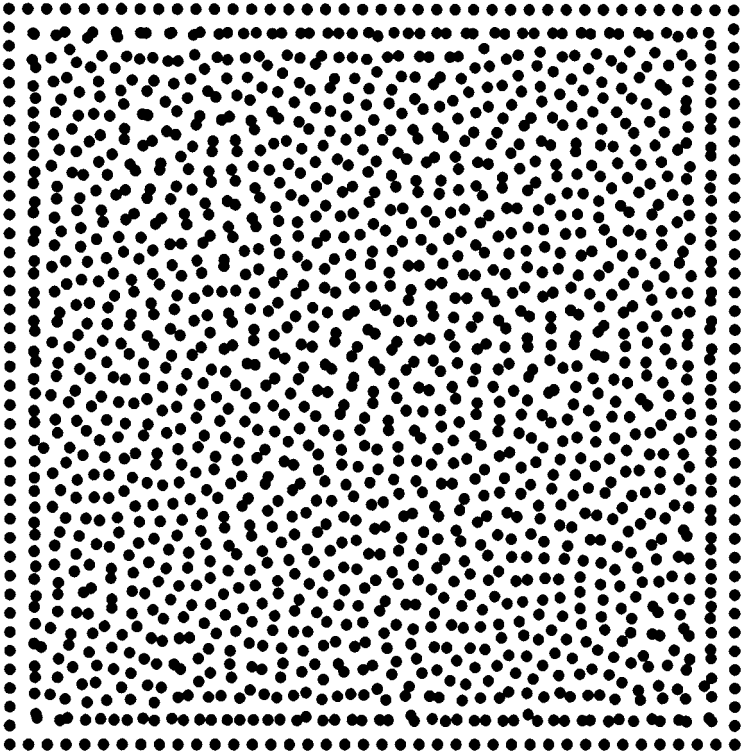
FIG. 25.   The particle positions for conduction is a slab modelled with disordered particles.

Figure 26 shows the temperature field at three different times. There is a close correspondence between the exact (curve) and SPH (point) solutions. The SPH simulation tracks the exact solution closely giving the correct spatial distribution and the correct temporal evolution of the temperature distribution. Comparing these to Figs. 13 and 23 we find that the disordered and ordered particles produce similarly accurate solutions. The spatial disorder of the particles introduces only a small amount of variation in the temperature profile. This appears as a slight spread of the SPH points around the exact solution. The magnitude of this variation is very small and does not increase (in absolute terms) with time. Importantly the SPH points are distributed evenly above and below the exact solution so that there is no consistent error in the mean underlying solution. The average error in the temperature begins at 0.13% and rises slowly to 0.91% at $t = 1.5$. The variation of the SPH points around the exact solution initially lies in the range 0.9 to 2.3%.

Figure 27 shows very close agreement between the exact (dashed line) and SPH (solid line) values of the average fluxes through the isothermal boundaries as a function of time. The initial and the peak errors are actually smaller for the disordered particles. The final errors are comparable. The average fluxes through the hot and cold walls have slightly different values initially (about 0.7%). This difference quickly vanishes as the temperature field adjusts to the disordered particle structure and the heat entering one side then fully balances the heat leaving the other. Overall, the average heat transfer rates are remarkably accurate for disordered particles in this configuration.

Similar tests using two-dimensional temperature distributions reveal similar accuracy when using disordered particles. This gives us substantial confidence in the ability of the
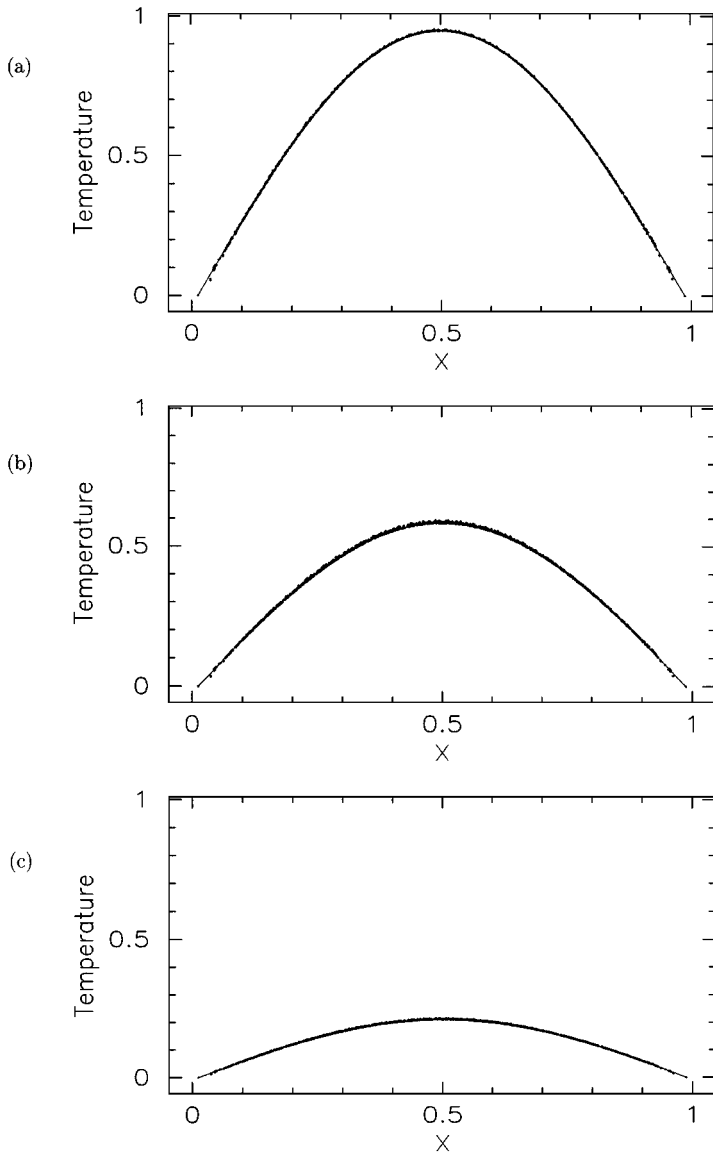
FIG. 26. The temperature profiles across the slab of disordered particles. The points indicate the SPH temperatures, whilst the curve shows the corresponding exact solution at each time (a) $t = 0.05$, (b) $t = 0.5$, and (c) $t = 1.5$.
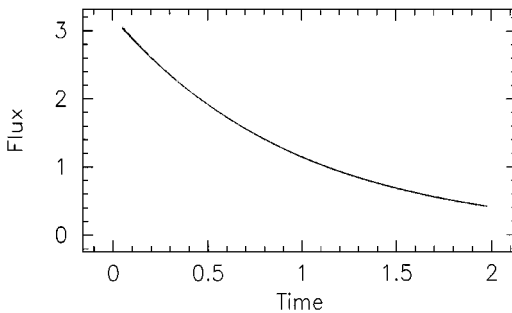
FIG. 27. Evolution of the SPH and exact average fluxes through the isothermal boundaries for the disordered particles.

this SPH formulation to correctly model conduction within fluids and between fluids and solids.

9. CONCLUSIONS

A form of the SPH energy equation has been developed that ensures continuity of heat flux across discontinuities in density, specific heat, and conductivity and when there are significant continuous spatial variations in material properties. A set of rules have been formulated for the construction of isothermal boundaries that lead to accurate solutions. Simulations of heat conduction in homogeneous slabs and discs and multi-material slabs were performed for a wide range of initial conditions. The predicted transient temperature distributions and heat fluxes through isothermal boundaries compare well with available exact solutions. In particular, the solution for an infinite material with a steep temperature discontinuity was found to be second order accurate. The inclusion of isothermal boundary conditions reduces the scheme to first order. Density corrections for the boundary particles were developed which improve the order of accuracy to 1.5 and also improve the accuracy of flux predictions. The level of accuracy at modest resolution is better than 1% for a wide range of problems with increasing complexity.

Specifically, we have found:

- The SPH methodology is very robust for modelling thermal conduction, since errors do not propagate or grow, but rather decay.
- The edges of solid materials are naturally adiabatic in the SPH formulation. Adiabatic boundaries do not affect the order of accuracy and result in only a marginal decrease in the actual level of accuracy.
- Total heat content is extremely well conserved in insulated materials.
- More than 10 particles in a region of large temperature variation is a sufficient number to predict the temperature distribution and its evolution with good accuracy.
- Conduction between materials of vastly different densities, specific heats, and conductivities can be accurately modelled. In particular, the solution for conduction between air and water is extremely accurate.
- Isothermal boundary conditions can be easily implemented in SPH by simply not undating the temperature or internal energy of the isothermal particles at each timestep.
- For slabs with isothermal sides, the solutions at early times agree closely with analytic solutions (when they exist).
- The asymptotic temperature profiles in slabs made from two materials with different conductivities are correctly predicted, as is the temperature at the interface.
- For materials with highly temperature-dependent conductivities the SPH solution is also very accurate.
- Isothermal boundary density corrections were obtained that improve the accuracy of the flux and temperature predictions of the SPH method and also increase the order of accuracy. For modest resolution the accuracy (compared to exact and *Fastflo* solutions) is better than 1%.
- Heat conduction calculations were performed using disordered particles in a range of one- and two-dimensional configurations, involving isothermal and adiabatic boundaries. The accuracy using these disordered particles varied between applications. In some cases the solutions (both temperature and heat flux) were more accurate for the disordered particles

than for the ordered particles. In other cases the reverse was true. In general the amount of variation was not large. This is a crucial test which benchmarks our formulation for fluid dynamical calculations.

- The particle spacing in the isothermal boundaries is crucial to ensuring its behaviour as a homogeneous isothermal boundary. Separations comparable to the interior particle grid spacing give excellent results.

- With a good implementation of the isothermal boundaries, the heat conduction is equally accurate whether parallel to the lines of particles or inclined to them, that is, the conduction simulations are not prejudiced by the directions of the particle grid.

REFERENCES

1. R. B. Bird, W. E. Stewart, and E. N. Lightfoot, *Transport Phenomena* (Wiley, New York, 1960).

2. L. Brookshaw, *The Stability of Binary Systems and Rotating Stars*, Ph.D. thesis, Department of Mathematics, Monash University, Clayton, 3169 (1986).

3. P. W. Cleary, *Conduction II: 2D Heat Conduction—Accuracy, Resolution and Timesteps*, SPH Technical Note #4, CSIRO Division of Mathematics and Stats, Tech. Report DMS-C 95/42 (1995).

4. P. W. Cleary, *Conduction III: 2D Heat Conduction—Example Problems*, SPH Technical Note #6, CSIRO Division of Mathematics and Statistics, Tech. Report DMS-C 95/43 (1995).

5. P. W. Cleary, Modelling confined multi-material heat and mass flows using SPH, *Appl. Math. Model.* (in press).

6. P. W. Cleary and J. J. Monaghan, *Conduction IV: Isothermal Boundary Conditions and Heat Fluxes*, SPH Technical Note #7, CSIRO Division of Mathematics and Statistics, Tech. Report DMS-C 95/87 (1995).

7. P. W. Cleary, *Conduction V: Heat Conduction with Disordered Particles*, SPH Technical Note #9, CSIRO Division of Mathematics and Statistics, Tech. Report DMS-C 95/96 (1996).

8. H. S. Carlsaw and J. C. Jaeger, *Conduction of Heat in Solids* (Oxford Univ. Press, London, 1965), 2nd ed. p. 87.

9. *Fastflo* Tutorial Guide, Numerical Algorithms Group Ltd, Jordan Hill Rd, Oxford, UK, OX2 8DR (1997).

10. S. Grilli, I. A. Svensen, and R. Subramanya, *J. Waterway Port Coastal Ocean Eng.* **123**, 102 (1997).

11. J. J. Monaghan, *Ann. Rev. Astron. Astrophys.* **30**, 543 (1992).

12. J. J. Monaghan, Simulating free surface flows with SPH, *J. Comp. Phys.* **110**, 399 (1994).

13. J. J. Monaghan and A. Kos, *Solitary Waves on a Cretan Beach*, Applied Mathematics reports, Monash University, 97/26 (1997).

14. J. J. Monaghan, *Conduction I: Heat Conduction with Discontinuous Conductivity*, SPH Technical Note #3, CSIRO Division of Mathematics and Statistics, Tech. Report DMS-C 95/85 (1995).